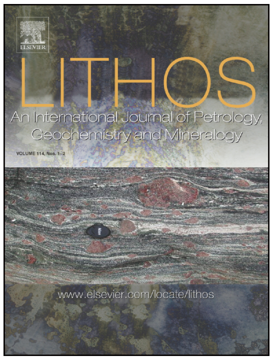

Apatite geochemistry as a tool for understanding the petrogenesis of layered mafic-ultramafic rocks in the Bushveld complex, South Africa

Peace Zowa, Ben Hayes, Grant Bybee, N. Alex Zirakparvar

PII: S0024-4937(25)00406-2

DOI: https://doi.org/10.1016/j.lithos.2025.108347

Reference: LITHOS 108347

To appear in: *LITHOS*

Received date: 8 April 2025

Revised date: 24 November 2025

Accepted date: 26 November 2025

Please cite this article as: P. Zowa, B. Hayes, G. Bybee, et al., Apatite geochemistry as a tool for understanding the petrogenesis of layered mafic-ultramafic rocks in the Bushveld complex, South Africa, *LITHOS* (2024), https://doi.org/10.1016/j.lithos.2025.108347

Apatite geochemistry as a tool for understanding the petrogenesis of layered mafic-ultramafic rocks in the Bushveld Complex, South Africa

Peace Zowa[1], Ben Hayes[1,2], Grant Bybee[1], and N. Alex Zirakparvar[3]

[1]School of Geosciences, University of the Witwatersrand, Johannesburg, South Africa

[2]CORES, School of Geosciences, University of the Witwatersrand, Johannesburg, South Africa

[3]Oak Ridge National Laboratory, Oak Ridge, Tennessee, United States of America

Correspondence: peacezowa96@gmail.com

Keywords: Apatite; Sr-Nd isotopes; Rustenburg Layered Suite; Isotopic disequilibrium.

Abstract

The sources of the magmas that formed the Rustenburg Layered Suite of the Bushveld Complex in South Africa remain debated, despite decades of research. Vertical and lateral variation in bulk rock and mineral separate Sr-Nd isotopic compositions, which generally indicate enriched sources, demonstrate that the layered sequence was formed by the emplacement of multiple batches of magma, crucially resulting in episodes of PGE-Cr-V mineralisation. The Lu-Hf isotope compositions of zircon are, however, at odds with the bulk rock Sr-Nd isotopic heterogeneity as they show near homogeneous compositions throughout the layered sequence ($\varepsilon Hf_{(2.06\ Ga)} = -8$). This lack of variation in Hf isotope composition has been attributed to deep, continental lithospheric mantle-related and/or crustal contamination of plume-derived Bushveld magmas. In this study, we analysed the major, trace element and Sr-Nd isotope geochemistry of apatite in the Rustenburg Layered Suite. Apatite occurs as an intercumulus mineral in the lowermost regions and a cumulus mineral in the uppermost regions of the layered sequence and can therefore be used to test existing models for the isotopic disequilibrium between bulk rock Sr-Nd and zircon Hf isotopic compositions. Apatite is largely chlorapatite in the lowermost regions and fluorapatite in the uppermost regions of the layered sequence. The Merensky Reef is unusual in that it comprises both chlorapatite and fluorapatite. Apatite throughout the layered sequence is generally unzoned and shows no evidence of late-stage alteration. Trace element data show that apatite is enriched in L/HREE, with common negative Eu-Sr anomalies. These trace element signatures are consistent with a magmatic origin for the apatite grains, with prior, or concurrent, plagioclase crystallization from the same melt. Variability in *in situ* Sr and Nd isotope compositions of apatite is recorded throughout the layered sequence with $\varepsilon Nd_{(2.06\ Ga)}$ compositions varying between -2.5 and -10.2 and initial $^{87}Sr/^{86}Sr$ compositions varying between 0.7079–0.7103 (for the Marikana dikes only). The variability in Sr-Nd isotope compositions of apatite is consistent with the bulk rock (and mineral separate) variation in Sr-Nd isotope compositions, suggesting apatite preserves primary magmatic compositions in the Rustenburg Layered Suite.

1 Introduction

The Rustenburg Layered Suite (RLS) of the Bushveld Complex in South Africa is the largest known layered mafic-ultramafic intrusion on Earth, and is host to exceptional examples of igneous layering, along with stratiform PGE-Cr-V ore deposits (Cawthorn, 2015). The RLS is an exceptional natural laboratory to study the processes of magmatic differentiation and crystal accumulation in magma chambers. Previous studies have reported on the magma emplacement mechanisms and how the igneous layering was assembled. Viewpoints range from the emplacement of magma batches into a magma-filled chamber (e.g., Cawthorn and Spies, 2003; Latypov et al., 2022) to the emplacement of magma batches into a semi-crystalline (mushy) or solid cumulate pile (e.g., Hayes et al., 2024; Maghdour-Mashhour et al., 2021; Mungall et al., 2016; Scoates et al., 2021; Yao et al., 2021). Regardless of the mechanism for the mode of magma emplacement, there is strong evidence in terms of radiogenic isotopic variations, specifically bulk rock Sr-Nd isotopes, that there was the episodic emplacement of magmas into the RLS (e.g., Beukes et al., 2021; Kruger, 1994; Magson et al., 2024; Roelofse and Ashwal, 2012; Sharpe, 1981). The enriched nature of the Sr-Nd isotope compositions indicates that there was contamination of mantle-derived magmas with either lithospheric mantle or crustal reservoirs.

In contrast to the heterogeneous Sr-Nd isotopic variations, the Lu-Hf isotopic composition of zircon, a late-stage accessory mineral, is relatively homogeneous throughout the entire RLS with an average $\varepsilon Hf_{(2.06\ Ga)}$ composition of -8 (e.g., VanTongeren et al., 2016; Zeh et al., 2020; Zirakparvar et al., 2014). This suggests there may be isotopic disequilibrium between the early formed primocrystic minerals (i.e., plagioclase and orthopyroxene) and the late-stage minerals, such as zircon, that fractionated from the pore melt trapped in the crystal mush. It was argued that the homogeneous Hf compositions are a product of deep, lithospheric mantle contamination of the asthenospheric mantle/plume-derived primary melts to the Bushveld Complex (Zirakparvar et al., 2014). The main line of argument here in favour of lithospheric mantle involvement was that each magma batch into the RLS would need to be contaminated with the same volume of crust to account for the near-homogeneous Hf composition of zircon. The involvement of lithospheric mantle in the petrogenesis, and metallogenesis, of the Bushveld Complex has also been documented in other studies (e.g., Richardson and Shirey, 2008). The alternative idea for the near-homogeneous Hf isotope profile is that multiple reservoirs were involved during the petrogenesis of the RLS, including the asthenospheric mantle, the lithospheric mantle and the crust (Zeh et al. 2020).

In this study, we investigated the geochemistry of apatite throughout the RLS to see if it records either homogeneous or heterogeneous isotopic compositions. Apatite is a valuable indicator of melt sources (Gregory et al., 2009) and the behaviour of rare earth elements (REE) and volatiles in magmatic systems (Belousova et al., 2002; Harlov, 2015; Pedersen et al., 2021; Piccoli and Candela, 2002; VanTongeren and Mathez, 2012; Webster and Piccoli, 2015; Yan et al., 2024, 2023). Apatite is also present as both an intercumulus and a cumulus phase in the RLS (VanTongeren and Mathez, 2012; Willmore et al., 2000), and it can therefore be used to provide insights into various stages of magma evolution. This is unlike zircon, which generally fractionates from the late-stage pore melt trapped in the crystal mush. The advancement of LA-MC-ICP-MS analytical techniques over the past decade allows for Sr-Nd isotopes in apatite to be routinely analysed. The geochemistry of apatite has previously provided constraints on the origin of the PGE mineralisation in the Merensky Reef (Willmore et al., 2000) as well as the origin of apatite-rich layers in the Upper Zone (VanTongeren and Mathez, 2012). We analysed the geochemical composition (major, trace and Sr-Nd isotopes) of apatite throughout the RLS for the same samples that were previously studied for zircon Hf isotopes (Zirakparvar et al., 2014). These data allow us to test the existing hypotheses for the origin of the homogeneous Hf isotopic composition of zircon. They also provide a window into the usefulness of apatite paragenesis for understanding the petrogenesis and metallogenesis of the RLS.

2 Geological Setting

The Bushveld Complex (BC) is a Paleoproterozoic (2.06 Ga) large igneous province in the northeastern part of South Africa that was emplaced into the stable Kaapvaal Craton (Cawthorn, 2015). The BC is subdivided into four main units, namely the Lebowa Granite Suite, Rashoop Granophyre Suite, Rooiberg Group and the Rustenburg Layered Suite (RLS) (Cawthorn, 2015). This paper focuses on the RLS, the mafic-ultramafic layered component of the BC, which hosts economically important magmatic ore deposits including the platiniferous Merensky Reef, UG-2 chromitite and Platreef (**Fig. 1**). The RLS covers an area of at least 100,000 km^2 and is exposed in three major limbs ranging in thickness between 5–9 km.

The RLS is subdivided into distinct units from the base upwards, namely the Marginal Zone, Lower Zone, Critical Zone, Main Zone and Upper Zone (Cawthorn, 2015: **Fig. 2**). The Marginal Zone (<500 m thick) consists of noritic and pyroxenite units. The Lower Zone (820–1390 m thick) is ultramafic, being dominated by orthopyroxenites, harzburgites and dunites. The Critical Zone is divided into lower and upper parts, with the lower part ultramafic in composition (780–800 m thick), dominated by orthopyroxenite and chromitite layering. The upper part (520–1000 m thick) is mafic-ultramafic in composition with macro-rhythmic pyroxenite, chromitite, norite and anorthosite layering. Stratiform PGE reefs, such as the Merensky Reef, are hosted in the upper part of the Critical Zone. The Main Zone (3100–2200 m thick) is the most volumetrically significant part of the RLS and is dominantly made up of gabbronorite. The Main Zone is locally crosscut by relatively evolved (gabbro–diorite) pegmatite dykes that are coeval and cogenetic to the RLS (Hayes et al., 2018). The Upper Zone (2000–2800 m thick) is mostly made up of ferrogabbros with local anorthositic layering (Cawthorn, 2015; Ver Hoeve et al., 2018). The Upper Zone also contains ~30 layers of magnetitite and nelsonite (a magnetite-ilmenite-apatite cumulate), ranging in thickness from 2 cm to >7 m, and which are globally significant resources of vanadium, titanium and phosphorus (Cawthorn and Molyneux, 1986; Von Gruenewaldt, 1993). Collectively, the various zones of the RLS are thought to have assembled over a time interval of ~5 Myr, between 2.06 and 2.055 Ga (Scoates et al., 2021).

3 Samples and Analytical Methods

Six samples used in this study are from the collection stored at the American Museum of Natural History that were studied for zircon Hf isotopes by Zirakparvar et al. (2014). Sample B07-40 was also studied in VanTongeren and Mathez, (2014). Two additional samples are from the Marikana Dykes (samples

MK1 and MK2) where zircon Hf isotope data were previously reported by Hayes et al. (2018). The list of samples used is presented in **Table 1**.

The samples were crushed, milled and sieved to different size fractions (<125 µm, 125–250 µm and >250 µm) in preparation for apatite separation using standard magnetic and heavy liquid mineral separation methods. The selection of individual apatite grains for geochemical analyses was based on the abundance, grain shape (preferably grains with no fractures), grain size (>60 µm), and purity (i.e., grains with no to little fluid or melt inclusions). Standard petrographic analyses were conducted at Wits University. Mineral modal abundances were estimated using the point counting method. Petrographic images were acquired using an Olympus BX63 full-scanning microscope and are presented in the **Supplementary Figures S1** file.

Bulk rock geochemical data were acquired for the samples used in this study. Major elements were determined using a Panalytical PW2404 X-ray fluorescence (XRF) spectrometer and trace elements were determined by inductively coupled plasma mass spectrometry (ICP-MS) using a Perkin Elmer Elan instrument in the Earth Lab at Wits University. Standard calibrations were made using synthetic oxide mixtures, international standard rocks, and in-house controls. BCR-1, BHVO-2 and BIR-1 were always run as unknowns. Primary external calibration standards were made up over the range of 5 – 100 ppb. Every ICP-MS determination was accompanied by control standards BCR-1, BHVO-1, and BIR-1 and for all elements, the deviation was less than 10% from the recommended values. The results of the standards are included with the full set of bulk rock data in **Supplementary Table 1.**

Cathodoluminescence (CL) and Backscattered Electron (BSE) imaging of the apatite grains was carried out using a TESCAN Integrated Mineral Analyser (TIMA) at Wits University on carbon-coated thin sections and apatite mounts to determine grain morphology, grain textures, the presence of melt or fluid inclusions, and the presence of chemical zoning. This process enabled us to select fresh and unaltered grains for analyses. The liberation analysis method was used to map the apatite grains using acquisition parameters of 7 µm pixel spacing, 15% minimum brightness, 100% maximum brightness, dot mapping X-ray resolution, 21 µm dot spacing, 500 µm field width, 1000 X-ray counts, 4 µs imaging speed, and a 100 % packing ratio. Images acquired using TIMA are presented in **Supplementary Figures S1**.

Quantitative compositional data for the apatite grains were obtained using a Cameca SX-100 electron microprobe at Spectrum at the University of Johannesburg. Measurements were obtained using four wavelength dispersive spectrometers. An accelerating voltage of 15 kV and a beam of 6 nA cup current were used for all analyses. The spatial resolution of the electron microprobe was 1–2 µm, and a beam diameter of 10 µm was used. Fluorine, Si, Cl, and Fe were counted first in every measurement to ensure accuracy and reliability, as this helps mitigate the effects of volatility, beam-induced damage and potential drift in analytical conditions. The raw electron microprobe data were corrected using the stoichiometric calculation method of Ketcham (2015). The instrument was calibrated using an in-house Phalaborwa apatite sample and acquired RSD% values of 0.95% and 1.30% for CaO and P_2O_5, respectively. The major elements were used to classify the types of apatite grains and to characterise any potential zoning. Over 140 analyses were carried out on over 100 apatite grains and are presented in full in **Supplementary Table S2**.

In situ trace element concentrations in apatite were determined by Laser Ablation Inductively Coupled Plasma Mass Spectrometry (LA-ICP-MS) using an Australian Scientific Instruments (ASI) 193 nm ArF Resolution SE excimer laser coupled to a Thermo Fisher iCAP RQ ICP-MS at Spectrum at the University of Johannesburg. Each measurement was acquired using single spot analyses (70–100 µm diameter depending on grain size), a repetition rate of 4 Hz, 50% beam attenuation, 2.3 J/cm^2 fluence and beam energy of 6 mJ. The total acquisition time was 65 seconds, comprising 15 seconds of pre-ablation and blank measurement followed by 50 seconds of measurement. Background signal was collected prior to ablation and subtracted from signal for background correction. Synthetic glass

NIST610 and NIST612 (Jochum et al., 2011) were used as external standards to calibrate the instrument, while Durango apatite (Yang et al., 2014) and USGS glass standard BCR-2G (Gao et al., 2002) were used as secondary standards and analysed as unknowns to evaluate the accuracy and precision of our measurements. The isotopes ^{7}Li, ^{23}Na, ^{29}Si, ^{43}Ca, ^{45}Sc, ^{49}Ti, ^{51}V, ^{52}Cr, ^{55}Mn, ^{56}Fe, ^{59}Co, ^{60}Ni, ^{69}Ga, ^{85}Rb, ^{89}Y, ^{91}Zr, ^{139}La, ^{140}Ce, ^{141}Pr, ^{146}Nd, ^{147}Sm, ^{151}Eu, ^{157}Gd, ^{159}Tb, ^{163}Dy, ^{165}Ho, ^{166}Er, ^{169}Tm, ^{174}Yb, ^{175}Lu, ^{178}Hf, ^{208}Pb, ^{232}Th and ^{238}U were all measured. Data reduction and processing were done using Glitter 4.5 software (Griffin et al., 2008), and ^{43}Ca was used as an internal standard, using the Ca values determined from the electron microprobe. Apatite grains in six samples were analysed with over 70 individual analyses conducted (**Supplementary Table S3**). The analytical uncertainties shown in supplementary table 3 are mostly within the expected range of values at 2σ level.

The Laser Ablation Multi Collector Inductively Coupled Plasma Mass Spectrometry (LA-MC-ICP-MS) at Spectrum at the University of Johannesburg was used to determine the Sr and Nd isotope compositions of apatite. The instrumentation consists of a Resolution 193 nm SE Excimer Laser Ablation system, connected to a Nu Plasma II MC-ICP-MS, with 16 Faraday detectors and 5 ion counting detectors. A plasma RF power of 1300 W was used with coolant Ar gas flow = 13.0 l/min, auxiliary gas flow = 0.80 l/min, nebuliser gas flow = 0.82 l/min and a laser He carrier gas flow of 0.31 l/min. Each measurement was done using a spot size ranging from 70 to 100 µm, depending on the signal and the size of the grain being analysed. A beam energy of 6 mJ, beam transmittance of 50 to 100 % (to obtain acceptable uncertainties), and a repetition rate of 7 Hz, resulting in an on-sample fluence of 2 to 6 J/cm^{2} were used for the analyses. Background correction was done by measuring the background signal on mass for 20 seconds prior to ablation, followed by 70 seconds of ablation, and then subtracting the background from the signal. For the Nd measurements, the instrument detectors were configured as follows; H5 = ^{150}Nd + ^{150}Sm; H4 = ^{149}Sm; H3 = ^{148}Nd + ^{148}Sm; H2 = ^{147}Sm; H1 = ^{146}Nd; Ax = ^{145}Nd; L1 = ^{144}Nd + ^{144}Sm; L2 = ^{143}Nd; L3 = ^{142}Nd + ^{142}Ce; L5 = ^{140}Ce. For the Sr measurements the detector set-up was as follow: H7 = ^{179}Hf2+; H6 = ^{178}Hf2+; H5 = ^{88}Sr + ^{176}Lu^{2+} + ^{176}Yb^{2+}; H4 = ^{175}Lu^{2+}; H3 = ^{87}Sr + ^{87}Rb + ^{174}Yb^{2+}; H2 = ^{173}Yb^{2+}; H1 = ^{86}Sr + ^{86}Kr + ^{172}Yb^{2+}; Ax = ^{171}Yb^{2+};

L1 = ^{85}Rb + ^{170}Yb^{2+} + ^{170}Er^{2+}; L3 = ^{84}Sr + ^{84}Kr + ^{168}Er^{2+} + ^{168}Yb^{2+}; L4 = ^{167}Er^{2+}; L5 = ^{83}Kr + ^{166}Er^{2+}; IC1 = ^{82}Kr + ^{164}Dy^{2+} + ^{164}Er^{2+}; IC2 = ^{163}Dy^{2+}. The following correction ratios were used ^{166}Er/^{167}Er = 1.4658, ^{168}Er/^{167}Er = 1.1679, ^{170}Er/^{167}Er = 0.6511, ^{168}Yb/^{171}Yb = 0.0091, ^{170}Yb/^{171}Yb = 0.2129, ^{172}Yb/^{171}Yb = 1.5287, ^{174}Yb/^{171}Yb = 2.21559, ^{176}Yb/^{171}Yb = 0.88395, ^{176}Lu/^{175}Lu = 0.02645, ^{164}Dy/^{163}Dy = 1.13212, ^{86}Sr/^{88}Sr = 0.1194 and ^{87}Rb/^{85}Rb = 0.3858. Details on how the mass bias correction and interference corrections were done can be found in Supplementary **Tables S4 and S5**. To assess the accuracy of the determined ratios, mass bias and interference corrections, secondary standards were measured as unknowns, including Durango (Doucelance et al., 2020), MAD, Mud Tank, Slyudyanka and McClure apatite (Yang et al., 2014), an in-house Phalaborwa apatite sample (Decrée et al., 2020), and the BHVO2G glass reference material (Raczek et al., 2003). These secondary standards were used to evaluate our measurement accuracy. The analytical uncertainties in our standards measurements fall within the published expected range of values. The measured values for Durango (^{87}Sr/^{86}Sr = 0.706369; ^{143}Nd/^{144}Nd = 0.512542), Mud Tank (^{143}Nd/^{144}Nd = 0.512394), Slyudyanka (^{87}Sr/^{86}Sr = 0.707690), McClure (^{87}Sr/^{86}Sr = 0.703724,) and BHVO2G (^{87}Sr/^{86}Sr = 0.703417) are in agreement with the recommended values of Durango (^{87}Sr/^{86}Sr = 0.70634; ^{143}Nd/^{144}Nd = 0.512490), Mud Tank (^{143}Nd/^{144}Nd = 0.512361), and Slyudyanka (^{87}Sr/^{86}Sr = 0.70769), McClure (^{87}Sr/^{86}Sr = 0.70371), and BHVO2G (^{87}Sr/^{86}Sr = 0.703435), respectively. Due to the difficulty in obtaining a reasonable number of apatite grains larger than 60 µm and their low resistance to ablation, only single analyses per grain were performed for isotopes and in situ trace elements. The limited recovery of apatite grains from the samples restricted the types of analyses that could be performed. As a result, *in situ* apatite Nd isotopic and trace element analyses were prioritised over Sr isotopic analyses. Apatite grains from sample LZ10-02 were too small to be analysed.

4 Results

4.1 Petrography

Sample B07-40 from the Upper Zone is an olivine and ilmenite-bearing diorite made up of plagioclase laths (70%), hornblende oikocrysts (15%), magnetite (5%), quartz (3%) and orthoclase (2%) (**Fig. 3a**). The accessory minerals (5%) in B07-40 include olivine, apatite, zircon, ilmenite, and chlorite. Samples MK1 and MK2 from the Marikana dikes are gabbro-diorites and are made up of coarse-grained, euhedral to subhedral plagioclase laths (65%), hornblende-pyroxene (15%), orthoclase (12%) and quartz (4%) (**Figs. 3b-c**). The accessory minerals (4%) include biotite, apatite, pyrite and ilmenite. Sample B90-01 from the Merensky Reef is a coarse-grained norite that is made up of subhedral calcic plagioclase (70%), orthopyroxene (15%), olivine (5%), clinopyroxene (2%), and anhedral quartz (3%) (**Fig. 3d**). The accessory minerals (5%) include apatite, biotite, ilmenite, magnetite, and hematite. Sample B90-07 from the Merensky Reef is a coarse-grained orthopyroxenite that is made up of euhedral to sub-euhedral orthopyroxene (60%), olivine (20%) plagioclase (15%), and minor clinopyroxene (3%) (**Fig. 3e**). The accessory minerals (2%) include apatite, chromite, chalcopyrite, biotite and actinolite. Sample B4 from the Upper Critical Zone is a coarse-grained anorthosite that is made up of euhedral plagioclase laths (90%), hornblende (5%) and clinopyroxene (3%) (**Fig. 3f**). The accessory minerals (2%) include zoisite, hematite and magnetite. Sample DT28 from the Upper Critical Zone is an orthopyroxenite that is made up of euhedral orthopyroxene (92%) and plagioclase (5%) with well-developed triple point junctions (**Fig. 3g**). The accessory minerals (3%) include apatite, biotite, chromite, quartz, hematite, and magnetite. Sample LZ10-02 from the Lower Zone is a medium-grained harzburgite that is made up of euhedral olivine (80%), orthopyroxene (10%), plagioclase (3%) and minor amounts of clinopyroxene (2%) (**Fig. 3h**). The accessory minerals (5%) include biotite, quartz, hematite, and magnetite.

4.2 Apatite grains

Apatite in the lowermost regions of the RLS occurs as an accessory mineral and is typically associated with late-stage, intercumulus minerals such as quartz, plagioclase, biotite, zircon, ilmenite, magnetite and hematite (**Fig. 4**). Apatite is most abundant in the Upper Zone as a cumulus phase (associated with plagioclase, ilmenite and magnetite) where it is euhedral and subhedral, with grain sizes ranging between 70 and 250 µm. The apatite grains show a range of sizes from 60 µm (in the Upper Zone) and up to 1000 µm (in the Upper Critical Zone). Backscattered electron and CL images show that the apatite grains are generally unzoned with only patchy to weak zoning locally observed (**Fig. 4**). Apatite from the Main Zone, Merensky Reef, and Upper Critical Zone is intercumulus and shows well-formed crystal faces (**Fig. 4**) and is typically easily recognised by its hexagonal shape. Some of the separated apatite grains have irregular, jagged and uneven shapes, which can be attributed to damage during the mineral separation process (**Fig. 5c, 5e, 5g**).

4.3 Bulk rock compositions and major elements in apatite

Bulk rock P_2O_5 contents for the RLS samples are as follows: B07-40 (0.54 wt.%), MK1 (0.23 wt.%), MK2 (0.14 wt.%), B90-01 (0.05 wt.%), B90-07 (0.02 wt.%), DT 28 (0.02 wt.%), and LZ10-02 (0.01 wt.%). Bulk rock compositions for these samples are provided in detail in the **Supplementary Table S1**. The major element compositions of apatite are shown in **Table 2,** and apatite classification, based on F-Cl-OH composition, is shown in **Fig. 6.** The complete dataset is presented in Supplementary Table S2. The P_2O_5 contents of apatite range between 38.06–41.21 wt.%, and CaO contents range between 51.97–54.50 wt.%, showing little variation, while SiO_2 contents range between 0.11–0.44 wt.%. Most of the apatite grains are fluorapatites with F contents ranging between 0.13–2.89 wt.%. The chlorapatites have Cl contents ranging between 0.12–5.98 wt.%. Apatite in the Upper Zone and Marikana Dykes is generally F-rich and is similar to apatite compositions in the Upper Zone reported in Willmore et al. (2000) and to apatite compositions in the Skaergaard intrusion (**Fig. 6**). Apatite in the Upper Critical Zone, including the Merensky Reef, is generally Cl-rich with some apatite grains extending towards OH and F-enrichment (**Fig. 6**). These compositions are generally comparable to published apatite compositions for the Critical Zone and Lower Zone (Willmore et al., 2000).

4.4 Trace elements in apatite

A summary of the trace element data for apatite is included in **Table 3**. Chondrite normalised rare earth elements (REE) patterns of apatite display enrichment in light rare elements (LREE) relative to heavy rare earth elements (HREE) (**Fig. 7**). Sr and Eu show negative anomalies (**Fig. 7**). Strontium concentrations range between 176–568 ppm, Eu concentrations range between 11–19 ppm, and Ce concentrations range between 1101–4216 ppm. Higher trace element concentrations were found in apatite grains in samples B90-01 and B90-07 from the Merensky Reef compared to the other samples.

4.5 Sr-Nd isotope geochemistry of apatite

The ^{143}Nd/^{144}Nd and ^{87}Sr/^{86}Sr ratios of apatite are shown in **Table 4**, and their variation as a function of stratigraphic height is shown in **Fig. 8**. The εNd$_{(2.06\ \mathrm{Ga})}$ composition of apatite in the samples ranges as follows: B07-40 (-6.18 ± 0.56 to -9.43 ± 1.98), MK1 (-4.44 ± 0.61 to -7.17 ± 0.82), MK2 (-2.48 ± 1.15 to -7.57 ± 1.02), B90-01 (-5.33 ± 0.42 to -9.05 ± 0.41), B90-07 (-8.74 ± 0.79 to -10.16 ± 0.89), and DT28 (-8.01 ± 0.30 to -8.83 ± 0.35). Only a single apatite grain was analysed in sample B4, which gave an εNd$_{(2.06\ \mathrm{Ga})}$ composition of -8.78 ± 0.87. Apatite grains from the Merensky Reef show a large range in εNd$_{(2.06\ \mathrm{Ga})}$ composition between -2.48 ± 0.99 to -10.16 ± 0.89 with an average εNd$_{(2.06\ \mathrm{Ga})}$ composition of -7 ± 1.4 (**Fig. 8**), as well as the most negative εNd$_{(2.06\ \mathrm{Ga})}$ composition. Initial ^{87}Sr/^{86}Sr$_{(2.06\ \mathrm{Ga})}$ values for apatite in MK1 and MK2 range from 0.7079 ± 0.0002 to 0.7103 ± 0.0004 and 0.7080 ± 0.0002 to 0.7089 ± 0.0002, respectively. Apatite in samples MK1 and MK2 display an average initial ^{87}Sr/^{86}Sr composition of 0.7090 ± 0.0004 and ^{87}Sr/^{86}Sr composition of 0.7085 ± 0.0022, respectively (**Fig. 8**).

5 Discussion

5.1 Paragenesis of apatite in the Rustenburg Layered Suite

We have characterised the spatial distribution and textural setting of apatite in different zones from the RLS. Generally, the abundance of apatite grains decreases down-section, with abundant cumulus apatite present in the Upper Zone and minimal intercumulus apatite present in the Lower Zone. The apatite grains throughout the RLS are mostly chemically homogeneous and range in shape from euhedral to subhedral. Intercumulus apatite is generally associated with a mineral assemblage consisting of plagioclase, quartz, biotite and K-feldspar (**Fig. 4**). This association indicates apatite crystallized late during the solidification of these cumulate rocks (e.g., Reynolds, 1985; Scoates and Wall, 2015; Willmore et al., 2000; Yudovskaya et al., 2013; Zeh et al., 2020, 2015). Apatite below the Upper Zone exhibits elongated and hexagonal crystal faces, habits interpreted to develop under near-equilibrium conditions (e.g., Webster and Piccoli, 2015). Apatite less commonly occurs with no well-formed crystal faces and in the lowermost regions of the RLS as an intercumulus phase that grew late in the magma(s) crystallization history.

The F content of apatite increases up-section in the RLS, while the Cl content decreases (**Fig. 6**). Apatite in the lowermost parts of the stratigraphy (i.e., in the Critical Zone and the Lower Zone) is typically chlorine-rich, although the Merensky Reef shows slight differences to this general pattern as it consists of both F- and Cl-rich apatite (**Fig. 6**). It is widely accepted that the Merensky Reef coincides with the influx of a chemically and isotopically distinct magma(s) into the RLS (Hamilton, 1977; Hayes et al., 2024; Kruger and Marsh, 1982). The existence of both F- and Cl-rich apatite in the Merensky Reef has also been interpreted to reflect an influx of chemically distinct hydrothermal fluids and/or melts (occurring above the crystallization temperature of 1000–1050°C for apatite) in a chemically evolving magma chamber (Boudreau et al., 1986; Boudreau and Kruger, 1990). The variation in halogen contents in the Merensky Reef may be a result of shifts in liquidus field boundaries caused by the gain or loss of volatile components from the melt (Boudreau and Kruger, 1990). Similar halogen variation is also observed in the Stillwater Complex and has been ascribed to a mixing event as Cl-rich vapour is exsolved from the solidifying footwall section and migrated up to mix with F-rich intercumulus and supernatant melts within olivine-bearing zone 1 which is host to the platiniferous J-M reef (Boudreau et al., 1986; Parker et al., 2022). It has therefore been suggested that the origin of the stratiform PGE reefs may in part be explained by Cl-rich hydrothermal fluids that have the potential to complex and redistribute base and precious metals from parts of the solidified cumulate pile.

The Upper Zone contains ~30 individual layers of magnetitite and nelsonite (a magnetite-ilmenite-apatite cumulate rock), ranging in thickness from 2 cm to over 7 m. These layers host globally significant deposits of V, Ti and P (Cawthorn and Molyneux, 1986; von Gruenewaldt, 1993). Models of liquid immiscibility have been proposed to explain the formation of the magnetitite and nelsonite layers in the Upper Zone. The REE concentrations in cumulus apatite from the Upper Zone were used to argue for large-scale separation of Si-rich and Fe-rich immiscible liquids (VanTongeren and Mathez, 2012). Although this immiscibility model was challenged with the REE concentrations instead interpreted as a product of crystal-melt re-equilibration in the solidifying crystal mush (Cawthorn, 2013a). In our study, trace element compositions for the Upper Zone (B07-40) do not reveal a distinctive geochemical break that is shown by VanTongeren and Mathez (2012), which has been used to suggest the occurrence of liquid immiscibility in the Upper Zone.

Bulk rock P_2O_5 contents exceeding 0.4 wt.% have been shown to be associated with cumulus apatite in the Upper Zone, while bulk rock contents of less than 0.1 wt.% are characteristic of intercumulus apatite below the Upper Zone (Tegner et al., 2006; Vantongeren et al., 2010; Willmore et al., 2000). We show that the cumulus nature of apatite in the Upper Zone is supported by bulk rock P_2O_5 contents in sample B07-40 (0.54 wt.%), which is greater than 0.4 wt.%. Instead, the intercumulus nature of apatite in the zones below the Upper Zone is supported by P_2O_5 contents less than 0.1 wt.% (as documented in section 4.3)

5.2 Primary magmatic compositions of apatite in the Rustenburg Layered Suite

The morphology of the apatite grains, being generally euhedral-subhedral, as well as the scarcity of mineral inclusions, indicates that the apatite grains were not affected by post-crystallization processes such as metamorphism or hydrothermal alteration (Webster and Piccoli, 2015). Rather, these habits, coupled with the lack of compositional zoning and recrystallization textures, suggest that the halogen concentrations reflect the relative abundances of the intercumulus melt at the time of apatite crystallization. This is important as it influences the reliability of the trace element and Sr-Nd isotope data, which will be discussed in the following sections.

Apatite trace element compositions have been demonstrated to be a valuable tool in petrogenetic research. Apatite biplots are very useful in distinguishing apatite from different rock types based on contents of Sr, Y, Mn, total REE, the degree of LREE enrichment and the size of the Eu anomaly (e.g., Belousova et al., 2002; O'Sullivan et al., 2020). Kieffer et al. (2024) demonstrated that apatite from orthopyroxene-bearing intrusions, including the RLS, has a high $(La/Nd)_N$ ratio (>1) and a low $(Gd/Yb)_N$ ratio (<6). We observed similar trends with $(La/Nd)_N$ values >1 and $(Gd/Yb)_N$ values generally <8 (**Fig. 9**). The apatite grains from the RLS are enriched in L/HREE with Ce/Yb_N ratios ranging between 7 and 25 with an average of 16 (n = 29) (**Fig. 10a**). Belousova et al. (2002) demonstrated that apatite with high chondrite Ce/Yb_N ratios is present in mafic and ultramafic rocks, whereas apatite compositions with lower Ce/Yb_N ratios are typically present in granitoids and dolerites. Our range of Ce/Yb_N ratios in apatite suggests these grains are primarily magmatic and formed from relatively evolved mafic to ultramafic melts.

The chondrite normalised apatite trace element patterns show negative Eu and Sr anomalies consistent with apatite signatures in mafic igneous rocks (see **Fig. 2** in O'Sullivan et al., 2020). Europium anomalies (Eu/Eu*) are dependent on the timing of apatite crystallization relative to feldspar (e.g., Tang et al., 2012) such that in feldspar-absent rocks like lherzolites or carbonatites, a weak negative Eu/Eu* is common and a strong negative Eu/Eu* in apatite from pegmatites and granitic rocks (Belousova et al., 2002). A negative Eu anomaly is visible in **Fig. 10b**, with Eu/Eu* values ranging from 0.11–0.55 (average of 0.28). The trace element patterns of apatite in the RLS do not compare to those of metasomatised apatite (**Fig. 2** in O'Sullivan et al., 2020), which typically has trace element compositions with low REE contents and high Sr contents as well as minor Eu anomalies (Chakhmouradian et al., 2017; O'Sullivan et al., 2020). Additionally, we note that if apatite in the RLS had experienced metasomatism, one would expect numerous inclusions of monazite and xenotime coupled with fluid-induced depletion of REEs (Harlov, 2015; Harlov et al., 2002). Instead, the apatite grains lack inclusions and complex zoning, showing relatively homogeneous textures in BSE images, suggesting the apatite is primarily magmatic in origin.

Studies have shown that apatite from mafic and ultramafic rocks systematically differ in trace element compositions from apatite in felsic granitoids (e.g., Belousova et al., 2002; O'Sullivan et al., 2020). The application of trace element compositional statistics using the machine learning method Support Vector Machine (SVM) in understanding apatite trace element compositions in various lithologies is a useful way of characterising apatite sources. We overlaid our data on the SVM plot in **Figure 11** and show that the RLS apatite plots in the mafic igneous rock (IM) field, reinforcing that these grains are magmatic in origin and from igneous mafic melts (O'Sullivan et al., 2020).

5.3 Petrogenetic constraints on the solidification of the Rustenburg Layered Suite from Sr-Nd isotopes in apatite

The $\varepsilon Nd_{(2.06\ Ga)}$ isotopic compositions of apatite in the RLS generally show variation as a function of stratigraphic height, with εNd values ranging from -2.5 to -10.2 (average = -7 ± 1.4; **Fig. 8**). The $\varepsilon Nd_{(2.06\ Ga)}$ values of apatite in the Upper Critical Zone are relatively more unradiogenic (average value of -8.5) when compared to bulk rock $\varepsilon Nd_{(2.06\ Ga)}$ values reported in Maier et al. (2000) and Magson et al. (2024). This may largely reflect mineral-scale isotopic disequilibrium between apatite and major silicate phases in the Merensky Reef, such as orthopyroxene and plagioclase. Disequilibrium in Nd isotopes between plagioclase and orthopyroxene has been reported (Prevec et al., 2005). Apatite in the Merensky Reef shows even more unradiogenic $\varepsilon Nd_{(2.06\ Ga)}$ values (up to -10.2 ± 0.9) similar to the most unradiogenic $\varepsilon Hf_{(2.06\ Ga)}$ values reported in zircon for the Merensky Reef (Zirakparvar et al.,2014; Zeh et al., 2020). This is also consistent with bulk rock trace element data showing that the Merensky Reef is generally more crustally contaminated compared with other parts of the Bushveld Complex (Arndt et al., 2005). The magmatic signatures of apatite, as constrained from its textures and trace element compositions, imply that the Sr-Nd isotopic compositions of apatite are primary magmatic signatures.

The isotopic chemistry of the Merensky Reef is even more complicated. Apatite $\varepsilon Nd_{(2.06\ Ga)}$ values reported here range from -7.2 to -10.2 and are broadly comparable to $\varepsilon Nd_{(2.06\ Ga)}$ values (-7.5 to -8.5) reported for orthopyroxene primocrysts in the Merensky Reef (Prevec et al., 2005). Conversely, plagioclase oikocrysts in the Merensky Reef have lower $\varepsilon Nd_{(2.06\ Ga)}$ values (-1.1 to -3.4) (Prevec et al., 2005). Strontium isotopes in plagioclase oikocrysts show enriched compositions and complex zoning patterns (e.g., Hayes et al., 2024). These mineral-scale isotope data generally show that the parental melts to these crystals had different contamination histories, with the orthopyroxene primocrysts likely delivered as a crystal cargo in the replenishing magma, and the plagioclase oikocrysts having crystallized from a separate melt in the crystal mush. The late-stage apatite composition may therefore reflect the isotopic composition of the final trapped pore melt with potentially late crustal contamination as suggested by Zeh et al. (2020). This may explain some of the more enriched Nd-Hf isotopic compositions of apatite and zircon in the Merensky Reef and may have been vital in aiding its PGE mineralization.

Strontium isotope compositions for apatite in the Marikana dikes have initial $^{87}Sr/^{86}Sr$ compositions varying between 0.7079 and 0.7103. These Sr isotopic compositions of apatite broadly overlap with the initial $^{87}Sr/^{86}Sr$ compositions reported for bulk rocks (and plagioclase feldspar separates) from the Upper Critical Zone and Main Zone (Bourdeau et al., 2021; Hayes et al., 2018; Kruger, 1994; Magson et al., 2024; Maier et al., 2000; Mangwegape et al., 2016). The isotopic compositions of the apatite grains from the Marikana dikes are interesting from different perspectives. These relatively evolved dykes were interpreted to have formed by the expulsion of fractionated melt from the underlying Critical Zone, with the dikes largely being a mixture of this fractionated melt and antecrysts of Main Zone gabbronorite (Hayes et al., 2018). The $\varepsilon Nd_{(2.06\ Ga)}$ isotopic composition of the apatite grains in the Marikana dikes ranges between -4.9 and -7.6 (average -5.8) and is comparable to the bulk rock $\varepsilon Nd_{(2.06\ Ga)}$ variations reported for the Main Zone, which is between -6.4 and -7.9 (Maier et al., 2000). The variation in Sr-Nd isotopes is best explained by periodic replenishment of the magma chamber and the mixing of isotopically distinct magmas. The variation in mineral Sr-Nd isotope compositions that are reported in different parts of the RLS suggests that the replenishing magmas were crystal-bearing (e.g., Chutas et al., 2012; Prevec et al., 2005; Yang et al., 2013). Strontium isotope compositions (initial $^{87}Sr/^{86}Sr$ = 0.7045–0.7085: Karykowski et al., 2017; Kruger, 1994; Wilson et al., 2017) and Nd isotope compositions ($\varepsilon Nd_{(2.06\ Ga)}$ = -5.3 to -7.9: Maier et al., 2000) indicate the involvement of different crustal reservoirs in the genesis of the RLS. Regardless of the melt source(s) for the RLS, these isotopic data lend support to the evidence of isotopic disequilibrium between the major silicate minerals in the RLS. Furthermore, it shows that the primocrystic mineral phases may be isotopically decoupled from the compositions of the accessory minerals in the same cumulate layer.

5.4 Testing hypotheses for the origin of homogeneous Hf isotope compositions in zircon in the Rustenburg Layered Suite

It has been shown that the Hf isotope composition of zircon is homogeneous throughout the RLS (VanTongeren et al., 2016; Zeh et al., 2020; Zirakparvar et al., 2014). Zirakparvar et al. (2014) interpreted the homogeneous Hf isotope compositions as evidence of sub-RLS levels of contamination, arguing that equal proportions of crustal contaminant for every magma batch would be required at the emplacement level of the RLS to explain these homogeneous compositions, which is unlikely. They also noted the key role played by the lithospheric root, with ultramafic material formed during the Ventersdorp large igneous province at c. 2.8 Ga contributing to the isotopic flavour of the primary melts to the Bushveld Complex. Zeh et al. (2020) similarly reported homogeneous zircon Hf compositions in the RLS, as well as in detrital and metamorphic zircons from the surrounding felsic rocks and Transvaal Supergroup metasediments. Zeh et al. (2020) suggested that the Hf isotopic composition of zircon was a function of contamination, but quoted three specific enriched reservoirs (asthenospheric mantle, enriched SCLM, and crust (lower/upper)), rather than solely the SCLM, consistent with the findings of Wilson et al. (2017). The role of crustal contamination in the petrogenesis of the RLS and the associated Lebowa Granite Suite was also emphasised by Skursch et al. (2022). Because metamorphic zircon in the Transvaal Supergroup has the same Hf isotope composition as zircon in the RLS, Zeh et al. (2020) suggested that the homogeneous Hf isotopic composition of the metamorphic zircon may have been influenced by late-fluid migration. Fluids would have been released during dehydration metamorphic reactions in the contact aureole, with Lu-Hf modified in the process. Therefore, the now homogeneous zircon Hf isotope profile could have initially been more varied because of the primary magmatic processes, as evidenced by the zircon morphologies and overgrowth textures, which Zeh et al. (2020) suggested to point to a heterogeneous flow in the contact aureole.

As intercumulus apatite also crystallizes from the late, fractionated (and hydrous) pore melt in the crystal mush, its isotopic composition can also be used to test these competing models presented by Zirakparvar et al. (2014) and Zeh et al. (2020). The Sr-Nd isotope compositions reported here are consistent with the bulk rock Sr-Nd variation that has been documented in the RLS (Kruger, 1994; Maier et al., 2000). It was argued that the Sr isotope compositions of the RLS are primary as most of the Sr would have been locked in plagioclase-orthopyroxene during early solidification, whereas the late timing of zircon saturation overlapped with the infiltration of late Zr-Hf-bearing fluids from the contact aureole (Zeh et al., 2020). Given that apatite, also a late-stage mineral, records comparable trends to the bulk rock Sr-Nd compositions, which are largely controlled by the primocrystic orthopyroxene and plagioclase mineral content, it suggests that there was minimal (or no) crustal contamination of the chamber during its crystallization. The petrogenesis of the PGE-enriched Merensky Reef may be an exception as it has more enriched isotopic and trace element compositions.

The apparent decoupling of Nd-Hf isotopic compositions of apatite and zircon in the RLS is highlighted in **Fig. 12** as these compositions do not lie parallel to the mantle array. This suggests there may be a process other than crustal contamination that controlled the Nd-Hf isotopic systematics of the RLS. Zeh et al. (2020) discuss the possibility of late fluid infiltration into the crystallizing mush and isotopic modification of zircon. It may be possible that zircon was preferentially affected by late-fluid flow whereas apatite was not. Apatite crystals retain primary Nd isotopic compositions until at least 500°C, with homogenisation of the Sm-Nd isotopic system occurring at apatite closure temperatures of ~600°C (e.g., Hammerli and Kemp, 2021; Yan et al., 2024). Recent studies show that although apatite chemistry can be disturbed (e.g. mostly by Cl-rich fluids), fluid chemistry is the main factor that controls the response of the Sm-Nd isotopic system to metasomatic alteration (Hammerli and Kemp, 2021; Li et al., 2022). It is possible that crustal fluid infiltration into the RLS at late stages in its solidification might have preferentially caused changes in the Lu-Hf isotope compositions and not the Sm-Nd isotope compositions. This means that apatite, in comparison to zircon, faithfully records the isotopic composition of late stage melts in the RLS.

6 Conclusion

In this study, we focused on the chemistry of apatite in different parts of the Rustenburg Layered Suite (RLS) and presented new *in situ* Sr-Nd isotopic, major and trace element data for this accessory mineral in order to test the models proposed for the origin of the homogeneous Hf isotopic compositions of zircon in the RLS. This study also provides constraints on the crystallization of the RLS using the paragenesis of apatite. Textural observations suggest that the intercumulus apatite in the lowermost parts of the RLS is an accessory phase that crystallized from the late-stage trapped melt with no evidence of metasomatic overprint from fluids. Textural observations and bulk rock P_2O_5 contents in the Upper Zone show that apatite formed as a cumulus phase. Furthermore, the *in situ* trace element compositions and discrimination diagrams show that apatite in the RLS is of magmatic origin. *In situ* $^{87}Sr/^{86}Sr_{(2.06\ Ga)}$ and $\varepsilon Nd_{(2.06\ Ga)}$ isotopic variations in apatite support the notion that the RLS was constructed from the emplacement of multiple, variably contaminated batches of magmas. The $\varepsilon Nd_{(2.06\ Ga)}$ composition of apatite is not in equilibrium with the $\varepsilon Hf_{(2.06\ Ga)}$ of zircon from the same samples in the RLS, according to the mantle array. Furthermore, the Sr-Nd isotopic compositions of apatite are comparable to the bulk rock and mineral separate variations in Sr-Nd recorded elsewhere in the RLS. These results show that the Sr-Nd isotopic composition of apatite faithfully records the isotopic composition of the late pore melt trapped in the crystal mush.

7 Acknowledgements

We are grateful to the American Museum of Natural History and Edmond A. Mathez for providing some of the samples that were used in this research. The support of the DSI-NRF Centre of Excellence (CoE) for Integrated Mineral and Energy Resource Analysis (DSI-NRF CIMERA) towards this research is hereby acknowledged. Opinions expressed and conclusions arrived at are those of the author(s) and are not necessarily to be attributed to the CoE. We sincerely thank Dr Nonkuselo Madlakana for her expertise and dedicated support in conducting TIMA analyses at Wits University. Henriette Ueckermann and Marlina Elburg provided invaluable guidance during the laser work at the University of Johannesburg. Special appreciation goes to Louis Mudalahothe for his mentorship in thin section preparation and his patient instruction in mineral processing techniques, including sample crushing, milling, and heavy-liquid separation. Two anonymous reviewers provided thoughtful feedback that has significantly improved the paper. The editorial handling of Gregory Shellnutt is also greatly appreciated.

8 References

Arndt, N., Jenner, G., Ohnenstetter, M., Deloule, E., Wilson, A.H., 2005. Trace elements in the Merensky Reef and adjacent norites Bushveld Complex South Africa. Mineralium Deposita 40, 550–575. https://doi.org/10.1007/s00126-005-0030-x

Belousova, E.A., Griffin, W.L., O'Reilly, S.Y., Fisher, N.I., 2002. Apatite as an indicator mineral for mineral exploration: trace-element compositions and their relationship to host rock type. Journal of Geochemical Exploration, 76, 45–69. https://doi.org/10.1016/S0375-6742(02)00204-2

Beukes, J., Roelofse, F., Gauert, C., Grobler, D., Ueckermann, H., 2021. Strontium isotope variations in the Flatreef on Macalacaskop, northern limb, Bushveld Complex: implications for the source of platinum-group elements in the Merensky Reef. Mineralium Deposita, 56, 45–57. https://doi.org/10.1007/s00126-020-00998-2

Boudreau, A.E., Kruger, F.J., 1990. Variation in the composition of apatite through the Merensky cyclic unit in the western Bushveld Complex. Economic Geology, 85, 737–745. https://doi.org/10.2113/gsecongeo.85.4.737

Boudreau, A.E., Love, C., Prendergast, M.D., 1995. Halogen geochemistry of the Great Dyke, Zimbabwe. Contributions to Mineralogy and Petrology, 122, 289–300. https://doi.org/10.1007/s004100050128

Boudreau, A.E., Mathez, E.A., McCallum, I.S., 1986. Halogen Geochemistry of the Stillwater and Bushveld Complexes: Evidence for Transport of the Platinum-Group Elements by Cl-Rich Fluids. Journal of Petrology, 27, 967–986. https://doi.org/10.1093/petrology/27.4.967

Bourdeau, J.E., Hayes, B., Zhang, S.E., Logue, A., Bybee, G.M., 2021. Origin and significance of noritic blocks in layered anorthosites in the Bushveld Complex, South Africa. Contributions to Mineralogy and Petrology, 177, 11. https://doi.org/10.1007/s00410-021-01872-8

Cawthorn, R., Molyneux, T., 1986. Vanadiferous magnetite deposits of the Bushveld Complex. Presented at the Mineral deposits of southern Africa, pp. 1251–1266.

Cawthorn, R.G., 2015. The Bushveld Complex, South Africa, in: Charlier, B., Namur, O., Latypov, R., Tegner, C. (Eds.), Layered Intrusions. Springer Netherlands, Dordrecht, pp. 517–587. https://doi.org/10.1007/978-94-017-9652-1_12

Cawthorn, R.G., 2013. Rare earth element abundances in apatite in the Bushveld Complex—A consequence of the trapped liquid shift effect. Geology, 41, 603–606. https://doi.org/10.1130/G34026.1

Cawthorn, R.G., Spies, L., 2003. Plagioclase content of cyclic units in the Bushveld Complex, South Africa. Contributions to Mineralogy and Petrology, 145, 47–60.

Chauvel, C., Lewin, E., Carpentier, M., Arndt, N.T., Marini, J.-C., 2008. Role of recycled oceanic basalt and sediment in generating the Hf–Nd mantle array. Nature Geoscience. 1, 64–67. https://doi.org/10.1038/ngeo.2007.51

Chu, M.-F., Wang, K.-L., Griffin, W.L., Chung, S.-L., O'Reilly, S.Y., Pearson, N.J., Iizuka, Y., 2009. Apatite Composition: Tracing Petrogenetic Processes in Transhimalayan Granitoids. Journal of Petrology, 50, 1829–1855. https://doi.org/10.1093/petrology/egp054

Decrée, S., Cawthorn, G., Deloule, E., Mercadier, J., Frimmel, H., Baele, J.-M., 2020. Unravelling the processes controlling apatite formation in the Phalaborwa Complex (South Africa) based on combined cathodoluminescence, LA-ICPMS and in-situ O and Sr isotope analyses. Contributions to Mineralogy and Petrology, 175. https://doi.org/10.1007/s00410-020-1671-6

Doucelance, R., Bruand, E., Matte, S., Bosq, C., Auclair, D., Gannoun, A.-M., 2020. In-situ determination of Nd isotope ratios in apatite by LA-MC-ICPMS: Challenges and limitations. Chemical Geology, 550, 119740. https://doi.org/10.1016/j.chemgeo.2020.119740

Gao, S., Liu, X., Yuan, H., Hattendorf, B., Günther, D., Chen, L., Hu, S., 2002. Determination of forty two major and trace elements in USGS and NIST SRM glasses by laser ablation-inductively coupled plasma-mass spectrometry. Geostandards Newsletter, 26, 181–196. https://doi.org/10.1111/j.1751-908X.2002.tb00886.x

Gregory, C.J., McFarlane, C.R.M., Hermann, J., Rubatto, D., 2009. Tracing the evolution of calc-alkaline magmas: In-situ Sm–Nd isotope studies of accessory minerals in the Bergell Igneous Complex, Italy. Chemical Geology, 260, 73–86. https://doi.org/10.1016/j.chemgeo.2008.12.003

Griffin, W.L., Powell, W.J., Pearson, N.J., O'Reilly, S.Y., 2008. GLITTER: data reduction software for laser ablation ICP-MS. Mineralogical Association of Canada, 308–311.

Hamilton, J., 1977. Sr Isotope and Trace Element Studies of the Great Dyke and Bushveld Mafic Phase and their Relation to Early Proterozoic Magma Genesis in Southern Africa. Journal of Petrology, 18, 24–52. https://doi.org/10.1093/petrology/18.1.24

Hammerli, J., Kemp, A.I.S., 2021. Combined Hf and Nd isotope microanalysis of co-existing zircon and REE-rich accessory minerals: High resolution insights into crustal processes. Chemical Geology, 581, 120393. https://doi.org/10.1016/j.chemgeo.2021.120393

Harlov, D.E., 2015. Apatite: A Fingerprint for Metasomatic Processes. Elements, 11, 171–176. https://doi.org/10.2113/gselements.11.3.171

Harlov, D.E., Förster, H.-J., Nijland, T.G., 2002. Fluid-induced nucleation of (Y + REE)-phosphate minerals within apatite: Nature and experiment. Part I. Chlorapatite. American Mineralogist, 87, 245–261. https://doi.org/10.2138/am-2002-2-306

Harlov, D.E., Andersson, U.B., Förster, H.-J., Nyström, J.O., Dulski, P., Broman, C., 2002. Apatite–monazite relations in the Kiirunavaara magnetite–apatite ore, northern Sweden. Chem. Phys. Accessory Miner. Cryst. Transform. Geochronoligical Appl. 191, 47–72. https://doi.org/10.1016/S0009-2541(02)00148-1

Hayes, B., Bybee, G.M., Mawela, M., Nex, P.A.M., van Niekerk, D., 2018. Residual Melt Extraction and Out-of-sequence Differentiation in the Bushveld Complex, South Africa. Journal of Petrology, 59, 2413–2434. https://doi.org/10.1093/petrology/egy101

Hayes, B., Maghdour-Mashhour, R., Ashwal, L.D., Smith, A.J., Ueckermann, H. and Vermeulen, J., 2024. Melt infiltration in a crystal mush and pegmatoid formation in the platiniferous Merensky Reef, Bushveld Complex, South Africa. Mineralium Deposita, 60(2), pp.237-259.

Hsieh, P.-S., Chen, C.-H., Yang, H.-J., Lee, C.-Y., 2008. Petrogenesis of the Nanling Mountains granites from South China: Constraints from systematic apatite geochemistry and whole-rock geochemical and Sr–Nd isotope compositions. Journal of Asian Earth Sciences, 33, 428–451. https://doi.org/10.1016/j.jseaes.2008.02.002

Ihlen, P.M., Schiellerup, H., Gautneb, H., Skår, Ø., 2014. Characterization of apatite resources in Norway and their REE potential — A review. Ore Geology Reviews, 58, 126–147. https://doi.org/10.1016/j.oregeorev.2013.11.003

Jochum, K.P., Weis, U., Stoll, B., Kuzmin, D., Yang, Q., Raczek, I., Jacob, D.E., Stracke, A., Birbaum, K., Frick, D.A., Günther, D., Enzweiler, J., 2011. Determination of Reference Values for NIST SRM 610–617 Glasses Following ISO Guidelines. Geostandards and Geoanalytical Research, 35, 397–429. https://doi.org/10.1111/j.1751-908X.2011.00120.x

Jones, R.E., van Keken, P.E., Hauri, E.H., Tucker, J.M., Vervoort, J., Ballentine, C.J., 2019. Origins of the terrestrial Hf-Nd mantle array: Evidence from a combined geodynamical-geochemical approach. Earth and Planetary Science Letters 518, 26–39. https://doi.org/10.1016/j.epsl.2019.04.015

Karykowski, B.T., Yang, S.-H., Maier, W.D., Lahaye, Y., Lissenberg, C.J., O’Brien, H., 2017. In situ Sr Isotope Compositions of Plagioclase from a Complete Stratigraphic Profile of the Bushveld Complex, South Africa: Evidence for Extensive Magma Mixing and Percolation. Journal of Petrology, 58, 2285–2308. https://doi.org/10.1093/petrology/egy008

Ketcham, R.A., 2015. Technical Note: Calculation of stoichiometry from EMP data for apatite and other phases with mixing on monovalent anion sites†. American Mineralogist, 100, 1620–1623. https://doi.org/10.2138/am-2015-5171

Kieffer, M.A., Dare, S.A.S., Namur, O., Mansur, E.T., 2024. Apatite Chemistry as a Petrogenetic Indicator for Mafic Layered Intrusions. Journal of Petrology, 65, egae022. https://doi.org/10.1093/petrology/egae022

Kruger, F.J., 1994. The Sr-isotopic stratigraphy of the western Bushveld Complex. South African Journal of Geology, 97, 393-398

Kruger, F.J., Marsh, J.S., 1982. Significance of 87Sr/86Sr ratios in the Merensky cyclic unit of the Bushveld Complex. Nature, 298, 53–55. https://doi.org/10.1038/298053a0

Latypov, R., Chistyakova, S., Barnes, S.J., Godel, B., Delaney, G.W., Cleary, P.W., Radermacher, V.J., Campbell, I., Jakata, K., 2022. Chromitite layers indicate the existence of large, long-lived, and entirely molten magma chambers. Scientific Reports, 12, 4092.

Latypov, R., Chistyakova, S., Barnes, S.J., Hunt, E.J., 2017. Origin of Platinum Deposits in Layered Intrusions by In Situ Crystallization: Evidence from Undercutting Merensky Reef of the Bushveld Complex. Journal of Petrology, 58, 715–761. https://doi.org/10.1093/petrology/egx032

Li, X.-C., Harlov, D.E., Zhou, M.-F., Hu, H., 2022. Experimental investigation into the disturbance of the Sm-Nd isotopic system during metasomatic alteration of apatite. Geochimica et Cosmochimica Acta, 330, 191–208. https://doi.org/10.1016/j.gca.2021.04.036

Maghdour-Mashhour, R., Hayes, B., Bolhar, R., Ueckermann, H., 2021. Sill Intrusion into Pyroxenitic Mush and the Development of the Lower–Upper Critical Zone Boundary of the Bushveld Complex: Implications for the Origin of Stratiform Anorthosites and Chromitites in Layered Intrusions. Journal of Petrology, 62, egaa090. https://doi.org/10.1093/petrology/egaa090

Magson, J., Roelofse, F., Bybee, G., Bolhar, R., 2024. The Merensky-Bastard interval at Hackney, eastern Bushveld Complex: results of a combined Sr–Nd-isotopic investigation. Contributions to Mineralogy and Petrology, 179, 72. https://doi.org/10.1007/s00410-024-02155-8

Magson, J., Roelofse, F., Bybee, G., Bolhar, R., 2023. Constraints on the Nd-isotopic composition and nature of the last major influx of magma into the Bushveld Complex. Contributions to Mineralogy and Petrology, 178, 14. https://doi.org/10.1007/s00410-023-01996-z

Maier, W.D., Arndt, N.T., Curl, E.A., 2000. Progressive crustal contamination of the Bushveld Complex: evidence from Nd isotopic analyses of the cumulate rocks. Contributions to Mineralogy and Petrology, 140, 316–327. https://doi.org/10.1007/s004100000186

Mangwegape, M., Roelofse, F., Mock, T., Carlson, R.W., 2016. The Sr-isotopic stratigraphy of the Northern Limb of the Bushveld Complex, South Africa. Journal of African Earth Sciences 113, 95–100. https://doi.org/10.1016/j.jafrearsci.2015.10.016

Mungall, J.E., Kamo, S.L. and McQuade, S., 2016. U–Pb geochronology documents out-of-sequence emplacement of ultramafic layers in the Bushveld Igneous Complex of South Africa. Nature Communications, 7(1), p.13385

O’Sullivan, G., Chew, D., Kenny, G., Henrichs, I., Mulligan, D., 2020. The trace element composition of apatite and its application to detrital provenance studies. Earth-Science Reviews, 201, 103044. https://doi.org/10.1016/j.earscirev.2019.103044

Parker, A.P., Clay, P.L., Boudreau, A.E., Burgess, R., O’Driscoll, B., 2022. Magmatic volatiles and platinum-group element mineralization in the Stillwater layered intrusion, U.S.A. American Mineralogist, 107, 797–814. https://doi.org/10.2138/am-2022-7982

Pedersen, J.M., Ulrich, T., Whitehouse, M.J., Kent, A.J.R., Tegner, C., 2021. The volatile and trace element composition of apatite in the Skaergaard intrusion, East Greenland. Contributions to Mineralogy and Petrology. 176, 102. https://doi.org/10.1007/s00410-021-01861-x

Piccoli, P.M., Candela, P.A., 2002. Apatite in Igneous Systems. Reviews in Mineralogy and Geochemistry, 48, 255–292. https://doi.org/10.2138/rmg.2002.48.6

Raczek, I., Jochum, K.P., Hofmann, A.W., 2003. Neodymium and Strontium Isotope Data for USGS Reference Materials BCR-1, BCR-2, BHVO-1, BHVO-2, AGV-1, AGV-2, GSP-1, GSP-2 and Eight

MPI-DING Reference Glasses. Geostandards Newsletter, 27, 173–179. https://doi.org/10.1111/j.1751-908X.2003.tb00644.x

Reynolds, I.M., 1985. Contrasted mineralogy and textural relationships in the uppermost titaniferous magnetite layers of the Bushveld Complex in the Bierkraal area north of Rustenburg. Economic Geology, 80, 1027–1048. https://doi.org/10.2113/gsecongeo.80.4.1027

Richardson, S.H., Shirey, S.B., 2008. Continental mantle signature of Bushveld magmas and coeval diamonds. Nature, 453, 910–913. https://doi.org/10.1038/nature07073

Roelofse, F., Ashwal, L.D., 2012. The Lower Main Zone in the Northern Limb of the Bushveld Complex—a >1·3 km Thick Sequence of Intruded and Variably Contaminated Crystal Mushes. Journal of Petrology, 53, 1449–1476. https://doi.org/10.1093/petrology/egs022

Scoates, J.S., Wall, C.J., 2015. Geochronology of Layered Intrusions, in: Charlier, B., Namur, O., Latypov, R., Tegner, C. (Eds.), Layered Intrusions. Springer Netherlands, Dordrecht, pp. 3–74. https://doi.org/10.1007/978-94-017-9652-1_1

Scoates, J.S., Wall, C.J., Friedman, R.M., Weis, D., Mathez, E.A., VanTongeren, J.A., 2021. Dating the Bushveld Complex: Timing of Crystallization, Duration of Magmatism, and Cooling of the World's Largest Layered Intrusion and Related Rocks. Journal of Petrology, 62. https://doi.org/10.1093/petrology/egaa107

Sha, L.-K., Chappell, B.W., 1999. Apatite chemical composition, determined by electron microprobe and laser-ablation inductively coupled plasma mass spectrometry, as a probe into granite petrogenesis. Geochimica et Cosmochimica Acta, 63, 3861–3881. https://doi.org/10.1016/S0016-7037(99)00210-0

Sharpe, M., 1981. The chronology of magma influxes to the eastern compartment of the Bushveld Complex as exemplified by its marginal border groups. Journal of the Geological Society, 138, 307–326.

Skursch, O., Corfu, F., Tegner, C., Lesher, C.E., Andreasen, R., Hagen-Peter, G.A. and Vervoort, J.D., 2022. Zircon U–Pb chronology and Hf isotopes of the Lebowa Granite Suite and petrogenesis of the

Bushveld Complex, South Africa. Contributions to Mineralogy and Petrology, 177(2), 26. https://doi.org/10.1007/s00410-022-01889-7

Sun, J.-F., Yang, J.-H., Wu, F.-Y., Li, X.-H., Yang, Y.-H., Xie, L.-W., Wilde, S.A., 2010. Magma mixing controlling the origin of the Early Cretaceous Fangshan granitic pluton, North China Craton: In situ U–Pb age and Sr-, Nd-, Hf- and O-isotope evidence. Lithos, 120, 421–438. https://doi.org/10.1016/j.lithos.2010.09.002

Sun, S.-S., McDonough, W.F., 1989. Chemical and isotopic systematics of oceanic basalts: implications for mantle composition and processes. Geological Society London, Special Publications, 42, 313–345.

Tang, M., Wang, X.-L., Xu, X.-S., Zhu, C., Cheng, T., Yu, Y., 2012. Neoproterozoic subducted materials in the generation of Mesozoic Luzong volcanic rocks: Evidence from apatite geochemistry and Hf–Nd isotopic decoupling. Gondwana Research, 21, 266–280. https://doi.org/10.1016/j.gr.2011.05.009

Tollari, N., Barnes, S.-J., Cox, R.A., Nabil, H., 2008. Trace element concentrations in apatites from the Sept-Îles Intrusive Suite, Canada — Implications for the genesis of nelsonites. Chemical Geology, 252, 180–190. https://doi.org/10.1016/j.chemgeo.2008.02.016

VanTongeren, J.A., Mathez, E.A., 2012. Large-scale liquid immiscibility at the top of the Bushveld Complex, South Africa. Geology, 40, 491–494. https://doi.org/10.1130/G32980.1

Vantongeren, J.A., Mathez, E.A., Kelemen, P.B., 2010. A Felsic End to Bushveld Differentiation. Journal of Petrology 51, 1891–1912. https://doi.org/10.1093/petrology/egq042

VanTongeren, J.A., Zirakparvar, N.A., Mathez, E.A., 2016. Hf isotopic evidence for a cogenetic magma source for the Bushveld Complex and associated felsic magmas. Lithos 248–251, 469–477. https://doi.org/10.1016/j.lithos.2016.02.007

Ver Hoeve, T.J., Scoates, J.S., Wall, C.J., Weis, D., Amini, M., 2018. A Temperature-Composition Framework for Crystallization of Fractionated Interstitial Melt in the Bushveld Complex from Trace

Element Systematics of Zircon and Rutile. Journal of Petrology, 59, 1383–1416. https://doi.org/10.1093/petrology/egy066

Vervoort, J.D., Plank, T., Prytulak, J., 2011. The Hf–Nd isotopic composition of marine sediments. Geochimica et Cosmochimica Acta 75, 5903–5926. https://doi.org/10.1016/j.gca.2011.07.046

Von Gruenewaldt, G., 1993. Ilmenite-Apatite Enrichments in the Upper Zone of the Bushveld Complex: A Major Titanium-Rock Phosphate Resource. International Geology Review 35, 987–1000. https://doi.org/10.1080/00206819309465570

Webster, J.D., Piccoli, P.M., 2015. Magmatic Apatite: A Powerful, Yet Deceptive, Mineral. Elements, 11, 177–182. https://doi.org/10.2113/gselements.11.3.177

Willmore, C.C., Boudreau, A.E., Kruger, F.J., 2000. The Halogen Geochemistry of the Bushveld Complex, Republic of South Africa: Implications for Chalcophile Element Distribution in the Lower and Critical Zones. Journal of Petrology, 41, 1517–1539. https://doi.org/10.1093/petrology/41.10.1517

Wilson, A.H., 2015. The Earliest Stages of Emplacement of the Eastern Bushveld Complex: Development of the Lower Zone, Marginal Zone and Basal Ultramafic Sequence. Journal of Petrology. 56, 347–388. https://doi.org/10.1093/petrology/egv003

Wilson, A.H., Zeh, A., Gerdes, A., 2017. In Situ Sr isotopes in Plagioclase and Trace Element Systematics in the Lowest Part of the Eastern Bushveld Complex: Dynamic Processes in an Evolving Magma Chamber. Journal of Petrology, 58, 327–360. https://doi.org/10.1093/petrology/egx018

Yan, X.-Y., Yang, D.-B., Xu, W.-L., Quan, Y.-K., Wang, A.-Q., Hao, L.-R., 2024. Controls on apatite compositional variations in magmatic rocks: A case study of Mesozoic mafic–felsic intrusions from the eastern North China Craton. Journal of Asian Earth Sciences, 265, 106111. https://doi.org/10.1016/j.jseaes.2024.106111

Yan, X.-Y., Yang, D.-B., Xu, W.-L., Quan, Y.-K., Wang, A.-Q., Hao, L.-R., Yang, H.-T., Wang, F., 2023. Apatite geochemistry from mafic rocks in the northeastern North China Craton: New insights into petrogenesis. Lithos, 436–437, 106942. https://doi.org/10.1016/j.lithos.2022.106942

Yang, S.-H., Maier, W.D., Lahaye, Y., O’Brien, H., 2013. Strontium isotope disequilibrium of plagioclase in the Upper Critical Zone of the Bushveld Complex: evidence for mixing of crystal slurries. Contributions to Mineralogy and Petrology 166, 959–974. https://doi.org/10.1007/s00410-013-0903-4

Yang, Y.-H., Wu, F.-Y., Yang, J.-H., Chew, D.M., Xie, L.-W., Chu, Z.-Y., Zhang, Y.-B., Huang, C., 2014. Sr and Nd isotopic compositions of apatite reference materials used in U–Th–Pb geochronology. Chemical Geology, 385, 35–55. https://doi.org/10.1016/j.chemgeo.2014.07.012

Yao, Z., Mungall, J.E., Jenkins, M.C., 2021. The Rustenburg Layered Suite formed as a stack of mush with transient magma chambers. Nature Communications, 12, 505. https://doi.org/10.1038/s41467-020-20778-w

Yudovskaya, M., Kinnaird, J., Naldrett, A.J., Rodionov, N., Antonov, A., Simakin, S., Kuzmin, D., 2013. Trace-element study and age dating of zircon from chromitites of the Bushveld Complex (South Africa). Contributions to Mineralogy and Petrology, 107, 915–942. https://doi.org/10.1007/s00710-013-0269-3

Zeh, A., Ovtcharova, M., Wilson, A.H., Schaltegger, U., 2015. The Bushveld Complex was emplaced and cooled in less than one million years – results of zirconology, and geotectonic implications. Earth and Planetary Science Letters, 418, 103–114. https://doi.org/10.1016/j.epsl.2015.02.035

Zeh, A., Wilson, A.H., Gudelius, D., Gerdes, A., 2020. Hafnium Isotopic Composition of the Bushveld Complex Requires Mantle Melt–Upper Crust Mixing: New Evidence from Zirconology of Mafic, Felsic and Metasedimentary Rocks. Journal of Petrology, egaa004. https://doi.org/10.1093/petrology/egaa004

Zirakparvar, N.A., Mathez, Edmond.A., Scoates, J.S., Wall, C.J., 2014. Zircon Hf isotope evidence for an enriched mantle source for the Bushveld Igneous Complex. Contributions to Mineralogy and Petrology, 168, 1050. https://doi.org/10.1007/s00410-014-1050-2

9 Tables and Figures

Fig. 1: A geological map showing the distribution of the major components of the Bushveld Complex and the locations of the samples used in this study (modified after Zirakparvar et al., 2014 and Latypov et al., 2017).

Fig. 2: A lithostratigraphic section through the Rustenburg Layered Suite and a detailed section through the Critical Zone – Main Zone contact (modified after Ver Hoeve et al., 2018). The maximum stratigraphic thicknesses of each Zone are shown with the values in regular font from the Western Limb and those in bold font from the Eastern Limb. The locations of the samples used in this study are shown by the stars.

Fig. 3: Representative photomicrographs, all in cross-polarised light, of the samples from which apatite was extracted; a) Upper Zone olivine ilmenite diorite (B07-40); b) Main Zone in contact with a Marikana Dyke gabbro-diorite (MK1); c) Marikana Dyke diorite (MK2); d). Merensky Reef norite (B90-01); e) Merensky Reef orthopyroxenite (B90-07); f) Upper Critical Zone anorthosite (B4); g) Upper Critical Zone orthopyroxenite (DT28); h) Lower Zone harzburgite (LZ10-02). Abbreviations: Ap, apatite; Ilm, ilmenite; Ol, olivine, Opx, orthopyroxene; Pl; plagioclase; Qz, quartz; Hbl, hornblende and Cpx, clinopyroxene; Hem, hematite.

Fig. 4: Backscattered electron and cathodoluminescence images of apatite grains in the samples selected for this study. (a-b). Subhedral to euhedral apatite in sample B07-40; (c-d). Intercumulus subhedral apatite grains in MK1 and MK2; (e-f). Intercumulus apatite grains associated with plagioclase and quartz in samples B90-07 and B90-01; (g-h). Elongate and hexagonal intercumulus apatite grains in samples B4 and DT28. Abbreviations: Ap, apatite; Bt, biotite; Mag, magnetite; Chr, chromite; Pl, plagioclase; Qz, quartz and Or, orthoclase.

Fig. 5: Backscattered electron and cathodoluminescence images of separated apatite grains in the samples selected for this study. (a) Euhedral and partly ragged apatite grains in sample B07-40; (b) Euhedral and subhedral, unzoned apatite grains in sample MK1; (c) Euhedral and unzoned apatite grains in sample MK2; (d) Weakly zoned euhedral apatite grain in sample B90-01; (e) Subhedral, unzoned

and partly fractured apatite grains in sample B90-07; (f) Euhedral and patchy apatite grain in sample B4; (g) Fractured and weakly zoned euhedral apatite grain in sample DT28; (h) Euhedral and patchy zoned apatite grain in LZ10-02.

Fig. 6: A Cl-F-OH ternary diagram showing the compositions of the apatite grains collected in this study and compared to other published data for apatite from the Rustenburg Layered Suite and the Skaergaard intrusion (modified after Willmore et al. 2000). Data for Skaergaard are from Boudreau et al. (1995) and Pedersen et al. (2021). The apatite major element compositions were normalised according to the method described in Ketcham (2015), which uses molar percentages.

Fig. 7: Chondrite normalised REE patterns for the apatite grains analysed in this study (shown as the coloured lines). The shaded region represents LA-ICP-MS analyses for apatite from previous studies conducted on mafic granitoids to igneous rocks (Belousova et al., 2001; Chu et al., 2009; Hsieh et al., 2008; Ihlen et al., 2014; Kieffer et al., 2024; Sha and Chappell, 1999; Tang et al., 2012; Tollari et al., 2008). Normalisation values are from Sun and McDonough (1989).

Fig. 8: The stratigraphic variation of $\varepsilon Nd_{(2.06\ Ga)}$ and initial $^{87}Sr/^{86}Sr_{(2.06\ Ga)}$ ratio of apatite analysed in this study. The boxes represent the range of values acquired for each sample, whilst the pink triangles represent the average εNd values. Due to the small sample size and limited apatite recovery in the RLS, only the Marikana Dykes samples had enough grains to perform both neodymium and strontium analyses. The stratigraphic column on the left is for illustrative purposes and is not to scale. Abbreviations: UZ, Upper Zone; MZ, Main Zone; UCZ, Upper Critical Zone; and LCZ, Lower Critical Zone.

Fig. 9: Plots showing a) the LREE $(La/Nd)_N$ and HREE $(Gd/Yb)_N$ ratios in $(Gd/Yb)_N$ and $(La/Nd)_N$ observed from this study (coloured shapes) and the intrusions previously discussed in Kieffer et al. (2024) represented as coloured dashed lines in the figure (The figure is modified after Kieffer et al (2024) and data plotted in this plot is from this study, Hagen-Peter et al. (2019); Hou et al. (2013); Luan et al. (2014); McBirney and Creaser (2003); Pedersen et al. (2021); She et al. (2016); Song et al. (2013); Tang et al. (2012); VanTongeren and Mathez (2012); Xing et al. (2014); Xing and Wang, (2017)); b)

the variations observed in the Sr/Y against Eu/Eu* multielement diagram for apatite analysed in this study which show europium anomalies that range from 0.1 to 0.8 and Sr/Y ratios from 0-4 for the BLIP intrusions and higher Sr/Y ratios for the Phalaborwa Complex (10-17). Fields defined in the figure are made up of data from this study (coloured symbols), Kieffer et al. (2024), Kieffer et al. (2023), Pedersen et al. (2021), Van Tongeren & Mathez (2012), Xing & Wang (2017), (She et al. (2016), and Xing et al. (2014); c) data from this study are displayed in the ternary discrimination diagram that combines EMPA and LA-ICP-MS data. The intercumulus and cumulus regions are defined from Kieffer et al. (2024). The Upper Zone (B07-40) apatite and some grains from Marikana Dykes (MK1) falls in the cumulus region, whereas, Marikana Dykes (MK2), Upper Critical Zone (B90-01 and B90-07) and Lower Zone (B4) fall in the intercumulus region as defined by Kieffer et al. (2024); d) a ternary plot highlighting variations observed in the Eu/Eu*, Sr/Y and (REE+Y)/10000 multielement ratio diagram for apatite analysed in this study. Our apatite data falls within the mafic region as defined by Kieffer et al. (2024).

Fig. 10: Apatite compositions from the RLS plotted on apatite discriminant diagrams: a) $(Ce/Yb)_N$ vs ∑LREE (La + Ce + Pr + Nd) and b) Y vs europium anomaly (Eu/Eu*). These discriminant plots show the composition fields of apatite from different rock types (modified after Belousova et al. (2002)).

Fig. 11: A support vector machine (SVM) categorisation scheme based on Sr/Y ratios vs light REE (La + Ce + Pr + Nd) for the apatite grains analysed in this study (modified after O'Sullivan et al. 2020). Key: UM= Ultramafic rocks including carbonatites, lherzolites and pyroxenites; ALK= Alkali rich igneous rocks; IM= mafic I-type granitoids and mafic igneous rocks; LM= lower- and medium-grade metamorphic and metasomatic; HM= partial-melts/leucosomes/high=grade metamorphic; S= S-type granitoids and high aluminium saturation index (ASI) 'felsic' I=types.

Fig.12: εHf and εNd values for zircon (Zirakparvar et al. 2014) and apatite (this study) from the Rustenburg Layered Suite are shown as coloured squares scattering around the mantle array, which is modified from Jones et al. (2019). A) shows a wider range of εNd and εHf values showing the key mantle endmembers (DMM, FOZO, HIMU, and EM), with EMI and EMII merged into one EM reservoir as a result of their similar isotopic compositions in these systems. B) Shows a larger-scale plot of the Nd-Hf diagram, focusing on our data points, relative to the mantle array. The Hf–Nd mantle array

is defined by the equation $\varepsilon Hf = 1.44\varepsilon Nd + 1.61$, which aligns with relationships reported in earlier studies (e.g., Chauvel et al., 2008; Vervoort et al., 2011).

Table 1. The samples used in this study are the same as those used in Zirakparvar et al. (2014) for the Rustenburg Layered Suite and Hayes et al. (2018) for the Marikana Dykes. The apatite present in the thin section for sample LZ10-02 were too small to analyse. The Upper Zone sample (B07-40) was previously analysed for apatite trace elements by VanTongeren and Mathez (2012). The trace element composition in this sample and several other samples from the same study were the subject of a comment-and-reply to discussion (Cawthorn 2013a, 2014; VanTongeren and Mathez, 2014). Note: *Drill core sample; **Underground sample.

Table 2: Average major element compositions (wt.%) for apatite in each sample. The number of spot analyses per sample is represented by *n*.

Table 3: Average trace element composition (in ppm) of the apatite grains analysed in this study for each sample.

Table 4: LA-MC-ICP-MS average measurements of Sr-Nd isotopes of apatite in our samples. This table also includes zircon εHf compositions for the same samples (calculated by Zirakparvar et al. (2014) and Hayes et al. (2018) and whole rock εNd values from Maier et al. (2000). *n* represents the number of grains analysed in this study.

Table 1

Sample ID	**Stratigraphic Location in the Rustenburg Layered Suite**	**Sub-unit**	**Latitude, Longitude**	**Number of Apatite Grains Recovered (this study)**	**Average εHf at 2.06 Ga of Zircon Grains in Zirakparvar et al. (2014)**	**Number of Zircon Grains Recovered in Zirakparvar et al. (2014)**
B07-40	Upper Zone	Subzone C ≈20 m below the top contact of the RLS	S 24° 51.794’ E 29° 50.634’	10	-6.8	19
MK1	Marikana Dykes	Crosscutting Subzone C of the Main Zone	S 25° 36.069’ E 27° 28.395’	15	-7.2	15
MK2	Marikana Dykes	Crosscutting Subzone C Main Zone	S 25° 36.069’ E 27° 28.395’	15	-8.8	11
B90-01	Upper Critical Zone	Tennis Ball Marker	S 24° 17.767’ E 29° 51.848’	17	-9.9	15
B90-07**	Upper Critical Zone	Merensky Reef	S 25°24.000’ E 29° 57.000’	5	-8.7	15
B4**	Upper Critical Zone	UG-2	S 25° 38.287’ E 27° 20.363’	1	-8.5	15
DT28*	Upper Critical Zone	UG-2	S 24° 17.136’ E 29° 49.377’	1	-9.0	8
LZ10-02	Lower Zone	-	S 24° 38.260’ E 30° 11.114’	0	-8.4	10

Table 2

Sample Name	**Zone**	***n***	**F**	**SiO_2**	**Cl**	**CaO**	**P_2O_5**	**FeO**	**BaO**	**Ce_2O_3**	**Nd_2O_3**	**La_2O_3**	**OH**	**Total**
B07-40	UZ	12	2.64	0.19	0.12	53.87	40.65	0.10	0.01	0.23	0.11	0.12	0.86	98.88
MK1	MZ	18	2.47	0.12	0.38	54.28	41.10	0.06	0.01	0.16	0.11	0.08	0.55	99.99
MK2	MZ	16	2.23	0.11	0.68	54.16	41.11	0.11	0.00	0.13	0.08	0.06	0.69	99.54
B90-01	MR	30	1.06	0.44	1.96	51.64	38.06	0.13	0.00	0.57	0.26	0.27	1.08	97.52
B90-07	MR	5	0.13	0.30	4.40	52.74	38.78	0.09	0.00	0.16	0.14	0.09	0.75	98.38
DT28-1	UCZ	1	0.20	0.21	5.98	51.97	38.28	0.05	0.00	0.43	0.22	0.13	0.07	97.53

Table 3

Sample	Zone	*n*	V	Sr	Y	Zr	La	Ce	Pr	Nd	Sm	Eu	Gd	Tb	Dy	Ho	Er	Tm	Yb	Lu	Hf	Th	U
B07-40	Upper Zone	6	0.2	256.6	640.0	1.4	922.8	1600.9	230.0	980.1	186.3	18.4	186.4	22.7	125.9	23.7	60.3	6.6	34.9	4.5	0.1	16.9	5.1
MK1	Crosscutting Main Zone	6	1.4	176.3	944.3	0.4	889.4	1802.3	281.7	1234.5	246.9	12.9	245.4	30.9	177.0	33.4	85.9	9.8	53.3	7.0	0.1	9.9	4.0
MK2	Crosscutting Main Zone	6	4.8	322.5	383.4	2.2	515.7	1114.0	144.5	611.2	116.3	19.0	110.9	13.4	74.1	13.7	34.4	3.8	20.4	2.8	0.1	32.7	9.9
B90-01	Merensky Reef	6	39.1	343.3	1043.3	2.0	1857.8	4215.7	584.8	2342.8	417.0	18.5	372.0	45.2	240.8	42.7	104.5	11.0	55.3	6.9	0.2	240.2	49.8
B90-07	Merensky Reef	4	30.3	568.4	473.5	0.6	585.4	1391.2	226.9	957.6	175.9	15.3	162.8	19.2	100.9	17.4	40.2	4.0	18.9	2.3	0.1	164.5	5.1
B4	Upper Critical Zone	1	32.6	310.2	525.1	17.7	429.0	1100.8	150.5	657.5	148.1	10.6	147.4	19.3	106.8	19.1	45.8	4.9	25.0	3.2	0.2	156.1	9.8

Table 4

Sample	Rock Name	Zone	*n*	εNd at 2.06 Ga of apatite (this study)	±2σ	$^{87}Sr/^{86}Sr$ at 2.06 Ga of apatite (this study)	±2σ	εHf at 2.06Ga of zircon (Zirakparvar et al., 2014)
B07-40	Olivine Ilmenite Diorite	Upper Zone	10	-7.10	4.54	-	-	-6.8
MK1	Diorite	Main Zone	15	-6.10	1.86	0.7090	0.0014	-7.2
MK2	Diorite	Main Zone	15	-5.89	5.35	0.7085	0.0006	-8.8
B90-01	Norite	Merensky Reef	17	-7.19	2.02	-	-	-9.9
B90-07	Orthopyroxene	Merensky Reef	4	-9.45	4.20	-	-	-8.7
B4	Anorthosite	Upper Critical Zone	1	-8.78	1.74	-	-	-8.5
DT28	Orthopyroxenite	Upper Critical Zone	3	-8.37	0.84	-	-	-9.0
LZ10-02	Harzburgite	Lower Zone	-	-	-	-	-	-8.4

Declaration of Competing Interest

The authors declare that they have no known competing financial interests or personal relationships that could have appeared to influence the work of this paper.

Highlights

Apatite in the Rustenburg Layered Suite is magmatic and reveals homogeneous texturesLower and Critical zone apatite is Cl-rich and F-rich in the Main and Upper zonesApatite trace elements reveal light LREE enrichment compared to HREESr-Nd isotopes in apatite show variability throughout the Rustenburg Layered Suite Apatite recorders the primary isotopic composition of the Bushveld Complex magmas

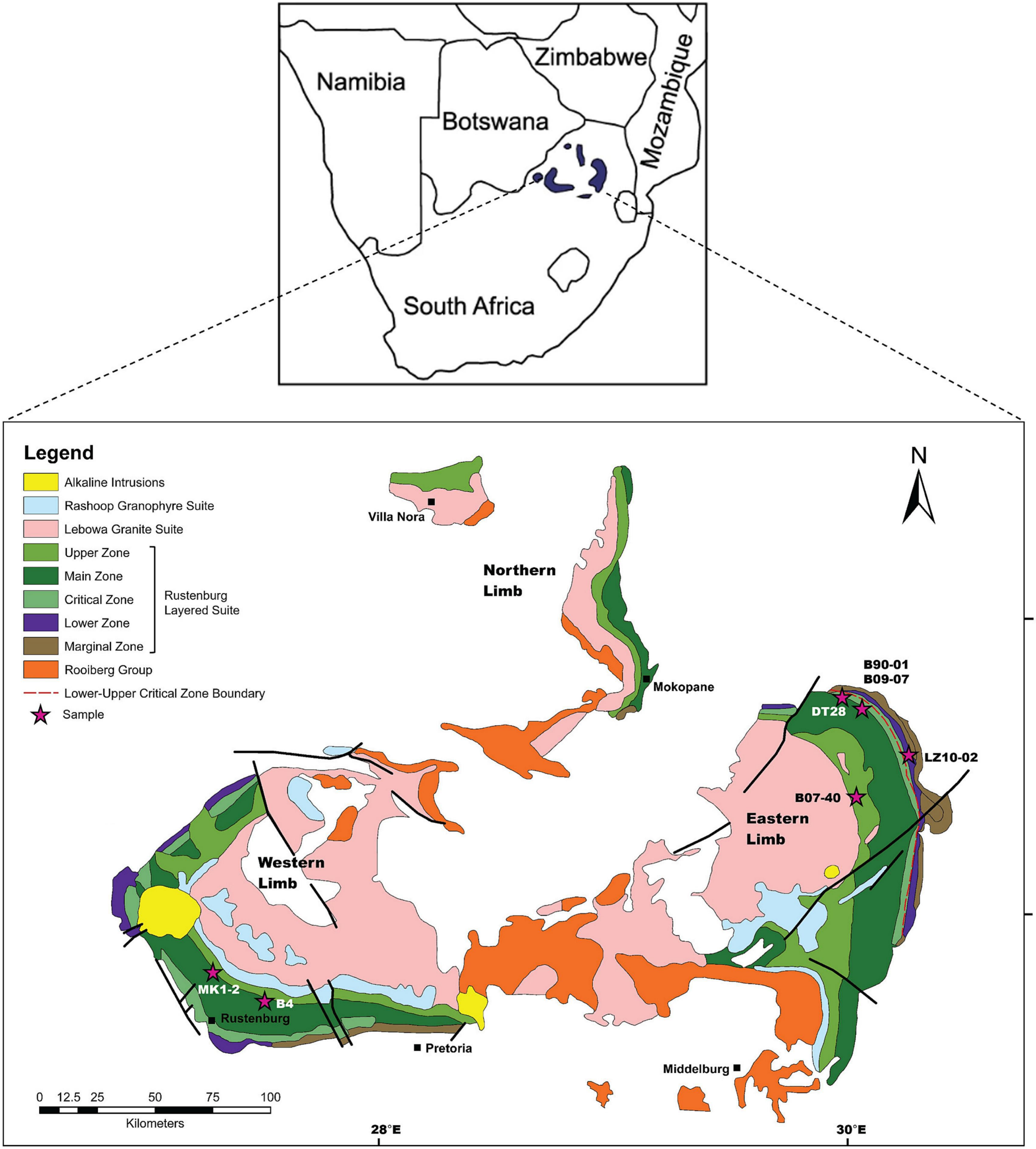
Namibia
Botswana
Zimbabwe
Mozambique
South Africa
Legend
Alkaline Intrusions
Rashoop Granophyre Suite
Lebowa Granite Suite
Upper Zone
Main Zone
Critical Zone
Lower Zone
Marginal Zone
Rustenburg Layered Suite
Rooiberg Group
Lower-Upper Critical Zone Boundary
Sample
N
Villa Nora
Northern Limb
Mokopane
24°S
B90-01
B09-07
DT28
LZ10-02
B07-40
Eastern Limb
Western Limb
25°S
MK1-2
B4
Rustenburg
Pretoria
Middelburg
0 12.5 25 50 75 100
Kilometers
28°E
30°E

Figure 1

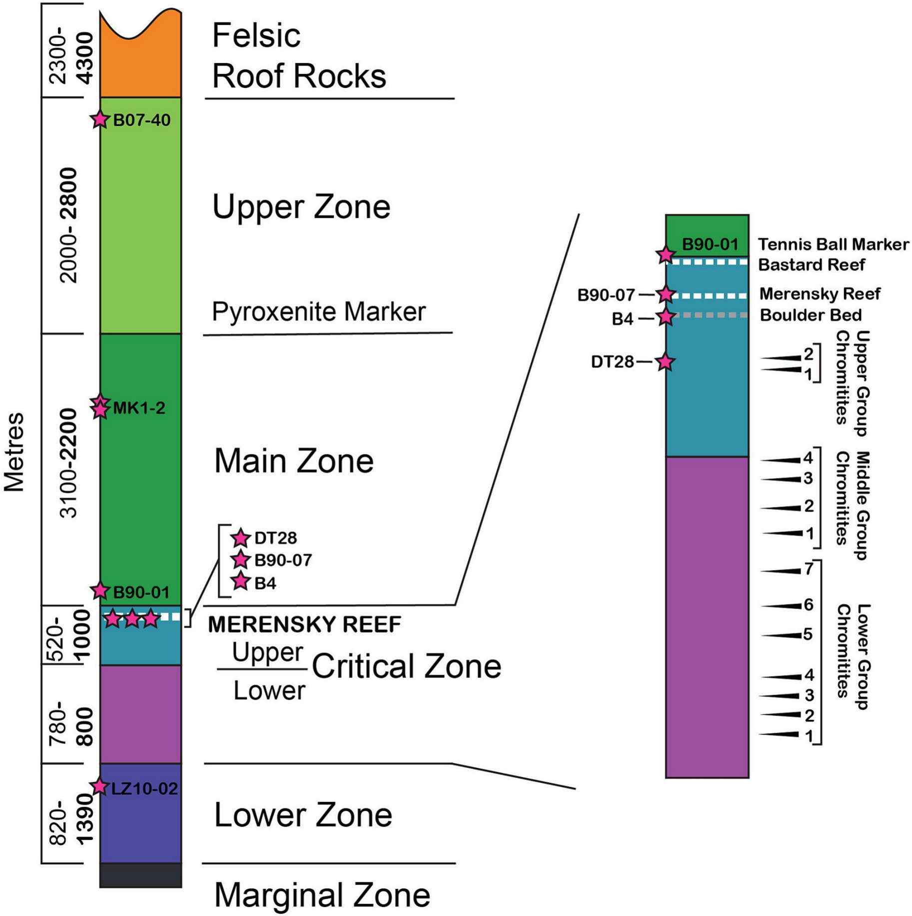
Metres
2300-4300
2000-2800
3100-2200
520-1000
780-800
820-1390
Felsic Roof Rocks
B07-40
Upper Zone
Pyroxenite Marker
MK1-2
Main Zone
B90-01
DT28
B90-07
B4
MERENSKY REEF
Upper
Critical Zone
Lower
LZ10-02
Lower Zone
Marginal Zone
B90-01
Tennis Ball Marker
Bastard Reef
B90-07
Merensky Reef
B4
Boulder Bed
DT28
Upper Group Chromitites
2
1
Middle Group Chromitites
4
3
2
1
Lower Group Chromitites
7
6
5
4
3
2
1

Figure 2

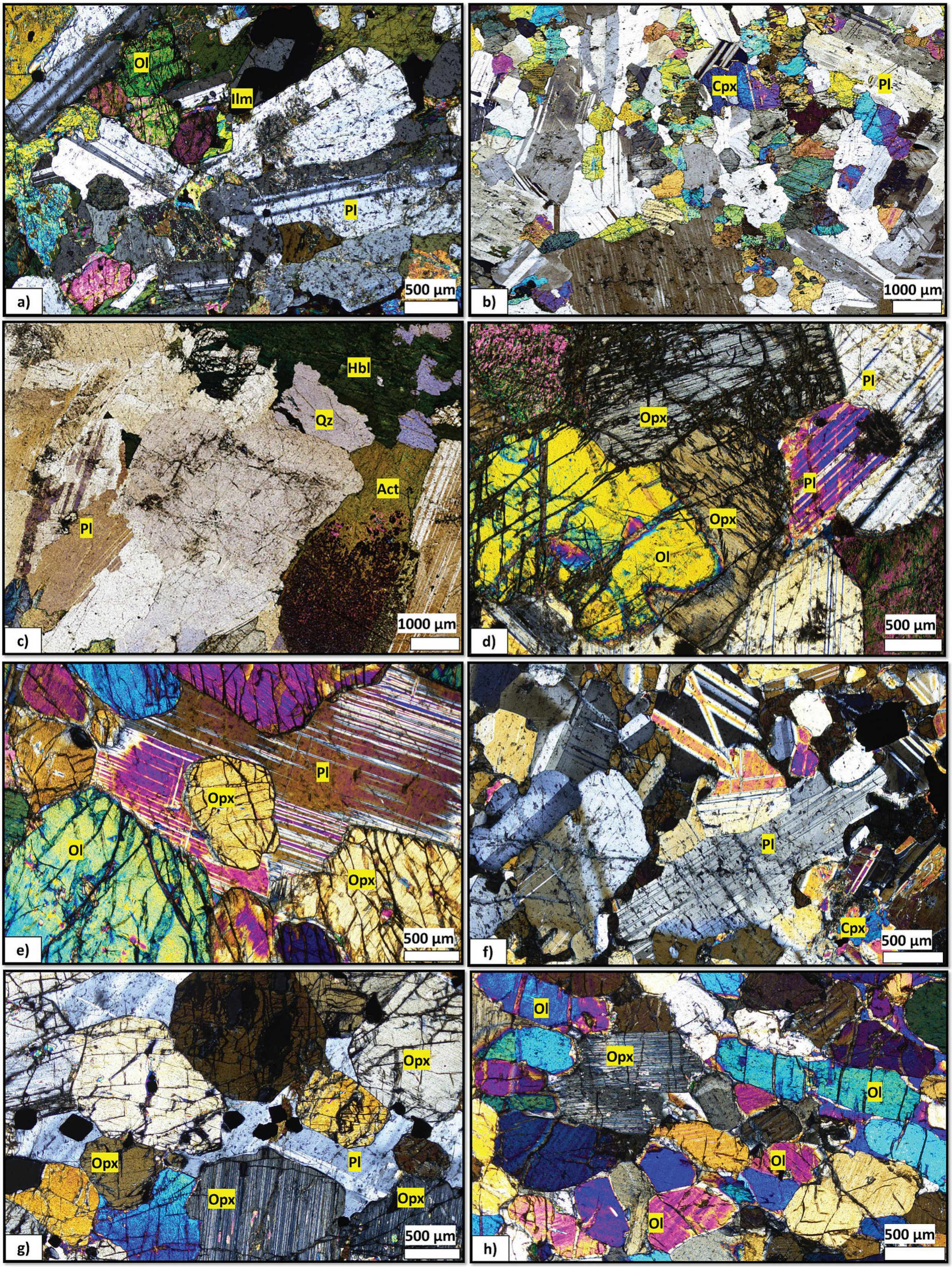
Ol
Ilm
Pl
500 µm
a)
Cpx
Pl
1000 µm
b)
Hbl
Qz
Act
Pl
1000 µm
c)
Opx
Pl
Pl
Opx
Ol
500 µm
d)
Pl
Opx
Ol
Opx
500 µm
e)
Pl
Cpx
500 µm
f)
Opx
Opx
Pl
Opx
Opx
500 µm
g)
Ol
Opx
Ol
Ol
Ol
500 µm
h)

Figure 3

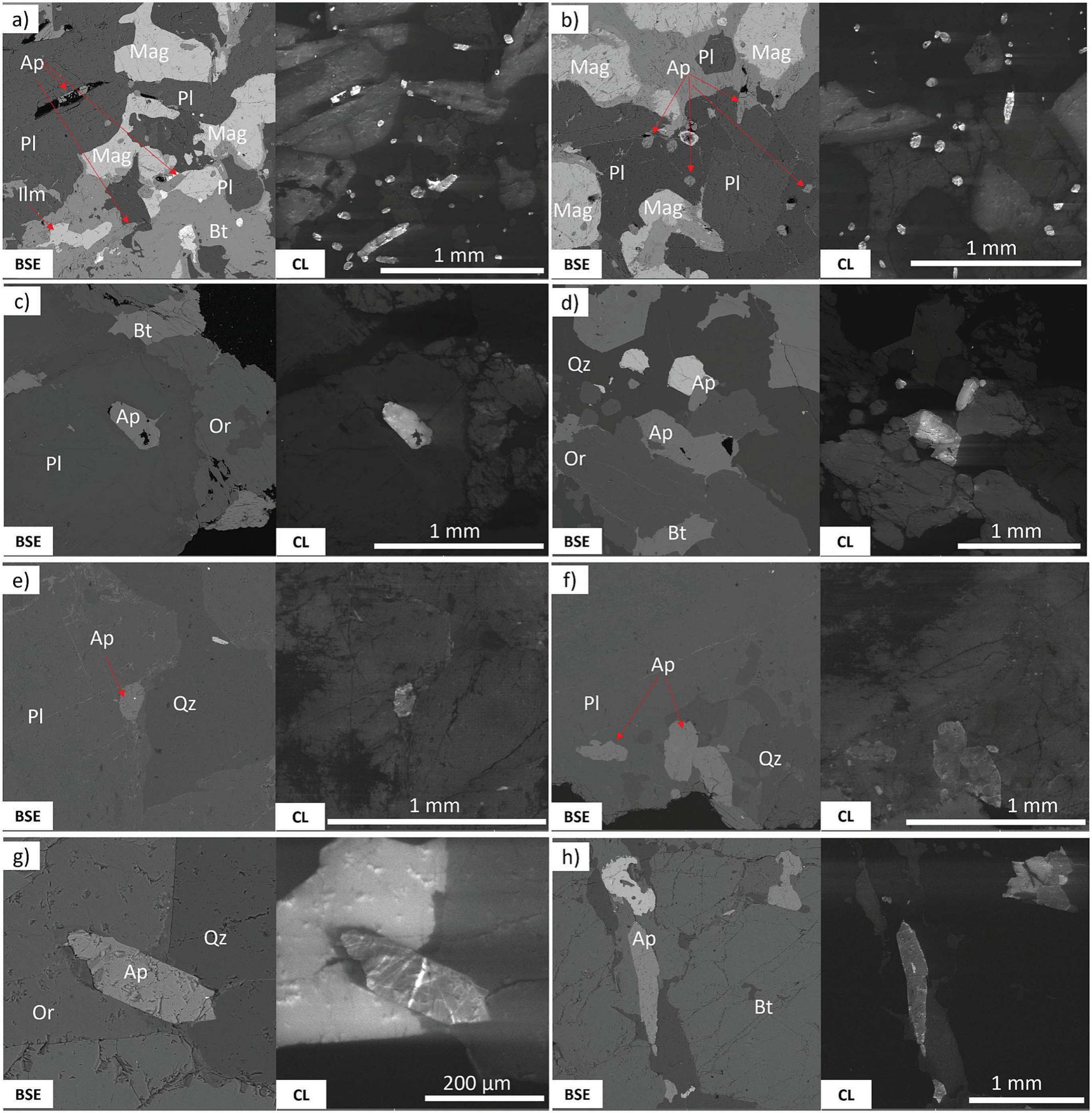
a)
Ap
Mag
Pl
Mag
Pl
Mag
Ilm
Pl
Bt
BSE
CL
1 mm
b)
Mag
Ap
Pl
Mag
Pl
Pl
Mag
Mag
BSE
CL
1 mm
c)
Bt
Ap
Or
Pl
BSE
CL
1 mm
d)
Qz
Ap
Ap
Or
Bt
BSE
CL
1 mm
e)
Ap
Pl
Qz
BSE
CL
1 mm
f)
Ap
Pl
Qz
BSE
CL
1 mm
g)
Qz
Ap
Or
BSE
CL
200 µm
h)
Ap
Bt
BSE
CL
1 mm

Figure 4

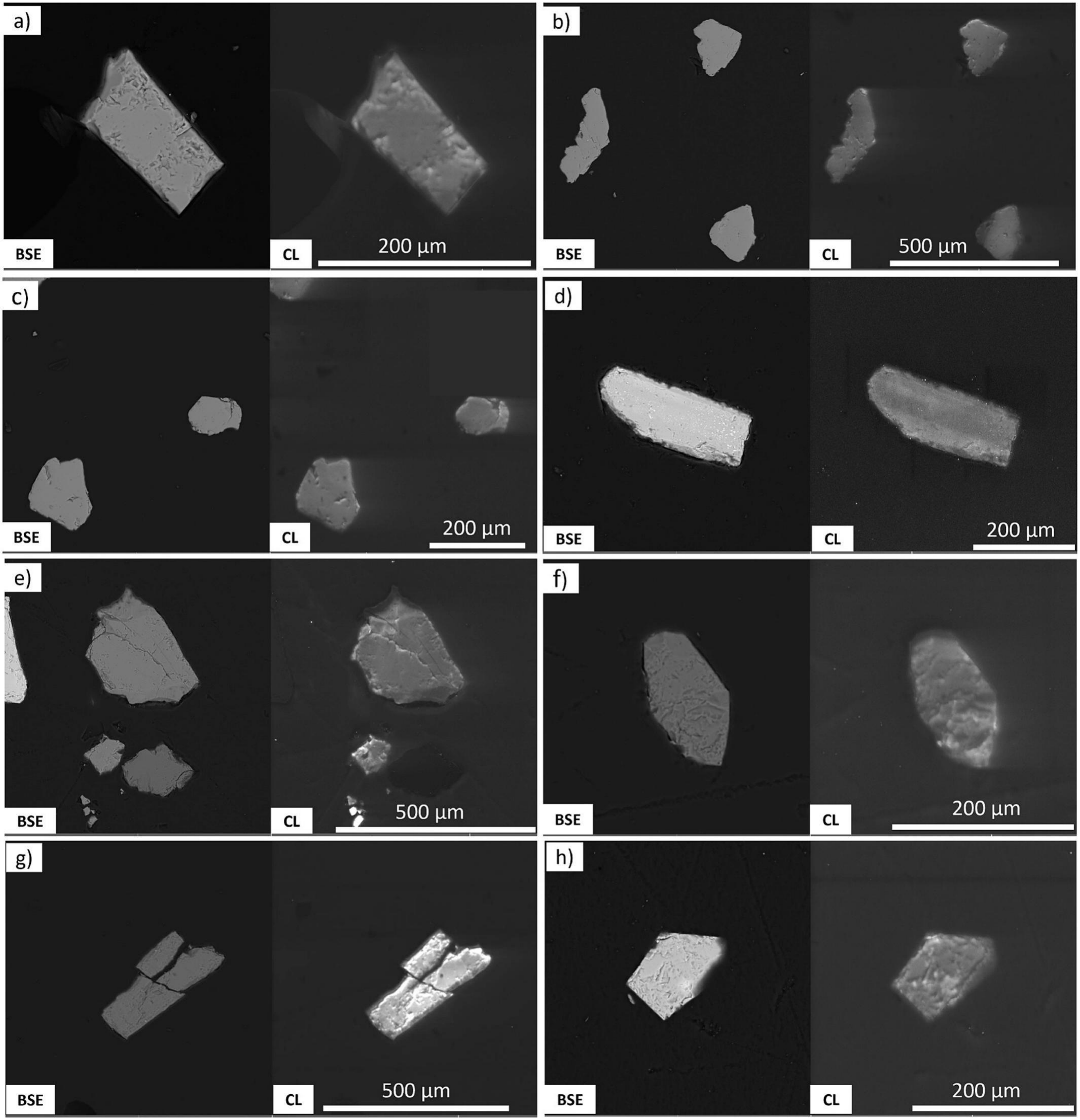
a)
BSE
CL
200 µm
b)
BSE
CL
500 µm
c)
BSE
CL
200 µm
d)
BSE
CL
200 µm
e)
BSE
CL
500 µm
f)
BSE
CL
200 µm
g)
BSE
CL
500 µm
h)
BSE
CL
200 µm

Figure 5

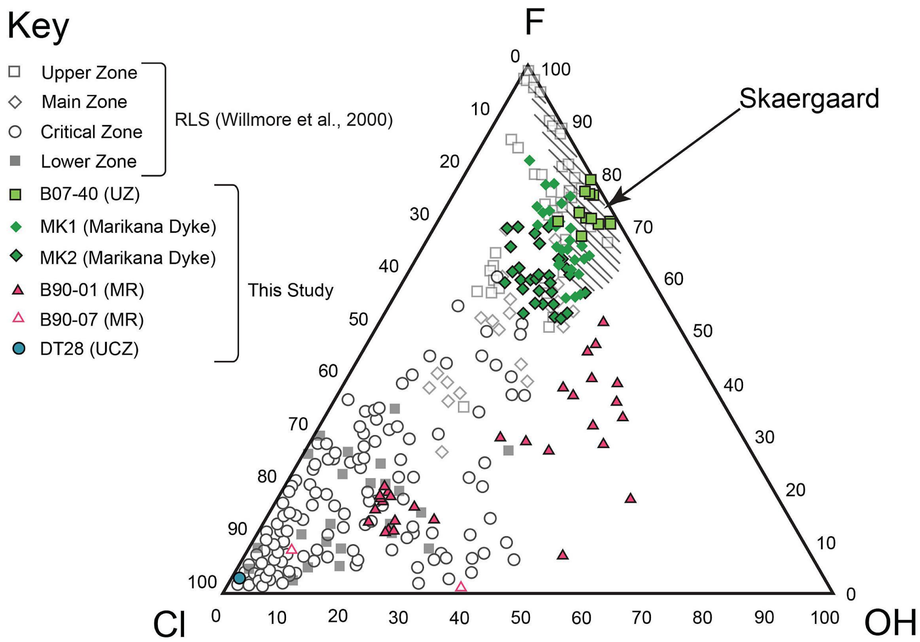
Key
□ Upper Zone
◇ Main Zone
○ Critical Zone
■ Lower Zone
RLS (Willmore et al., 2000)
🟩 B07-40 (UZ)
◆ MK1 (Marikana Dyke)
◆ MK2 (Marikana Dyke)
▲ B90-01 (MR)
△ B90-07 (MR)
● DT28 (UCZ)
This Study
F
Skaergaard
Cl
OH
0
10
20
30
40
50
60
70
80
90
100
100
90
80
70
60
50
40
30
20
10
0
0
10
20
30
40
50
60
70
80
90
100

Figure 6

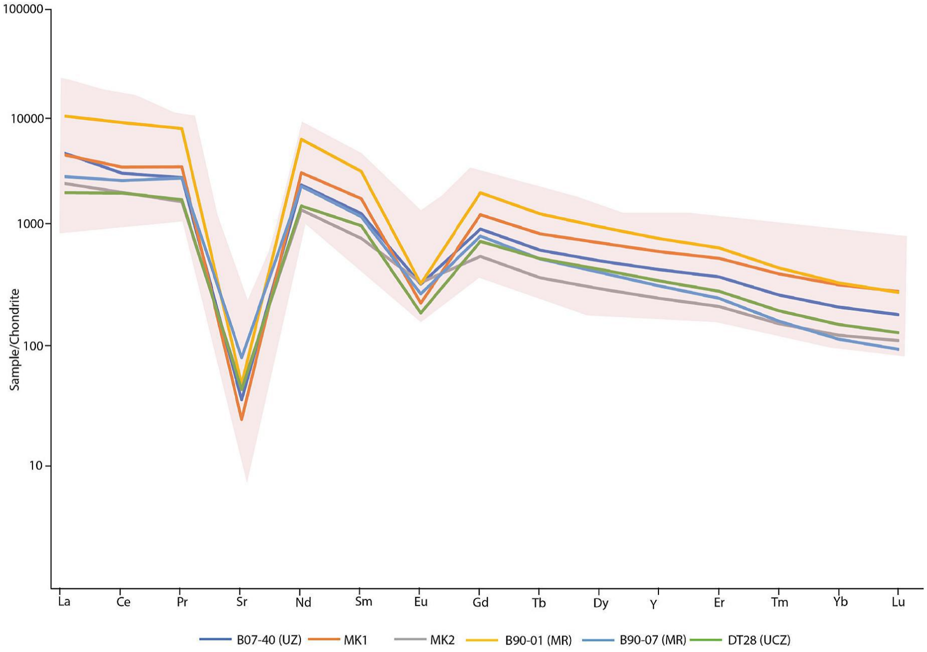
100000
10000
1000
100
10
Sample/Chondrite
La
Ce
Pr
Sr
Nd
Sm
Eu
Gd
Tb
Dy
Y
Er
Tm
Yb
Lu
B07-40 (UZ)
MK1
MK2
B90-01 (MR)
B90-07 (MR)
DT28 (UCZ)

Figure 7

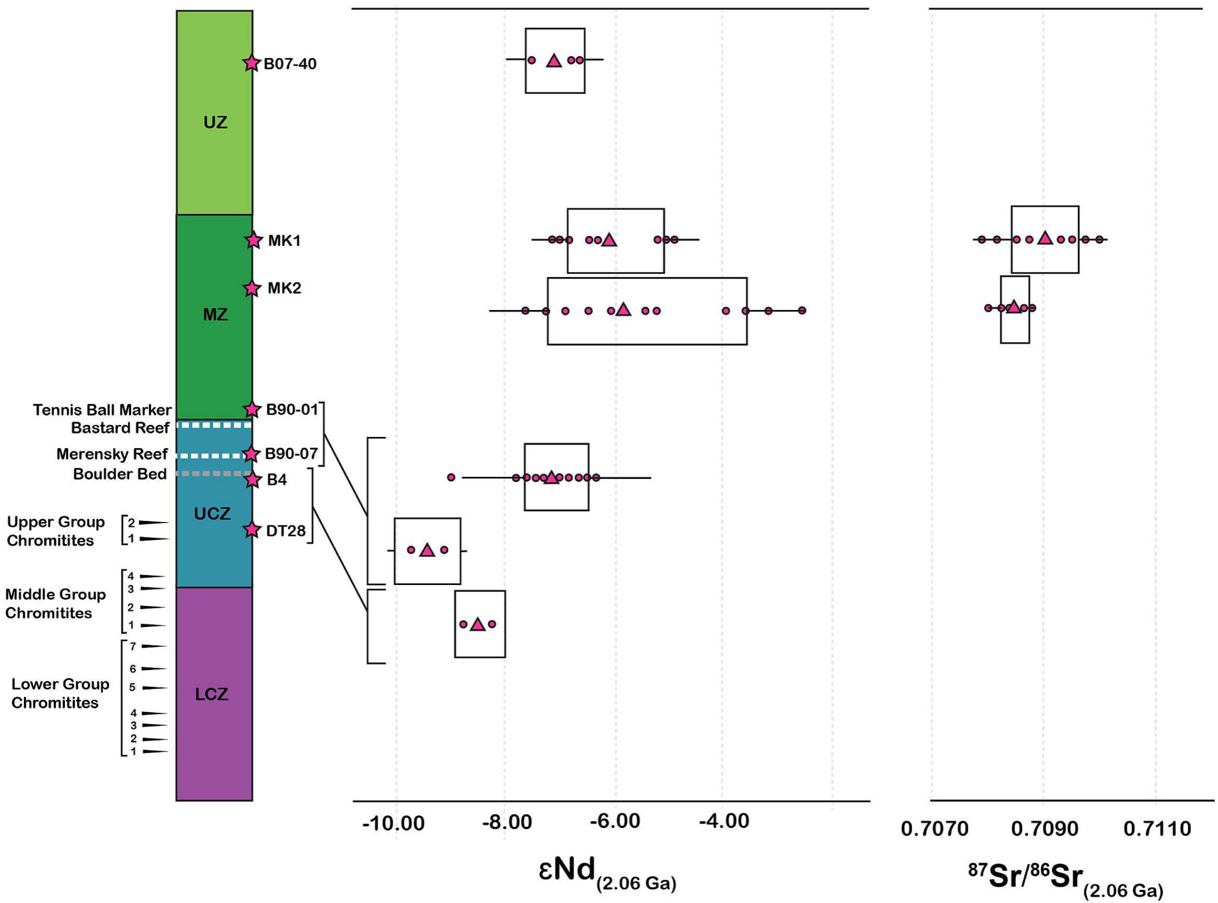
B07-40
UZ
MK1
MK2
MZ
Tennis Ball Marker
Bastard Reef
B90-01
Merensky Reef
B90-07
Boulder Bed
B4
UCZ
Upper Group Chromitites
2
1
DT28
Middle Group Chromitites
4
3
2
1
Lower Group Chromitites
7
6
5
4
3
2
1
LCZ
-10.00
-8.00
-6.00
-4.00
εNd(2.06 Ga)
0.7070
0.7090
0.7110
87Sr/86Sr(2.06 Ga)

Figure 8

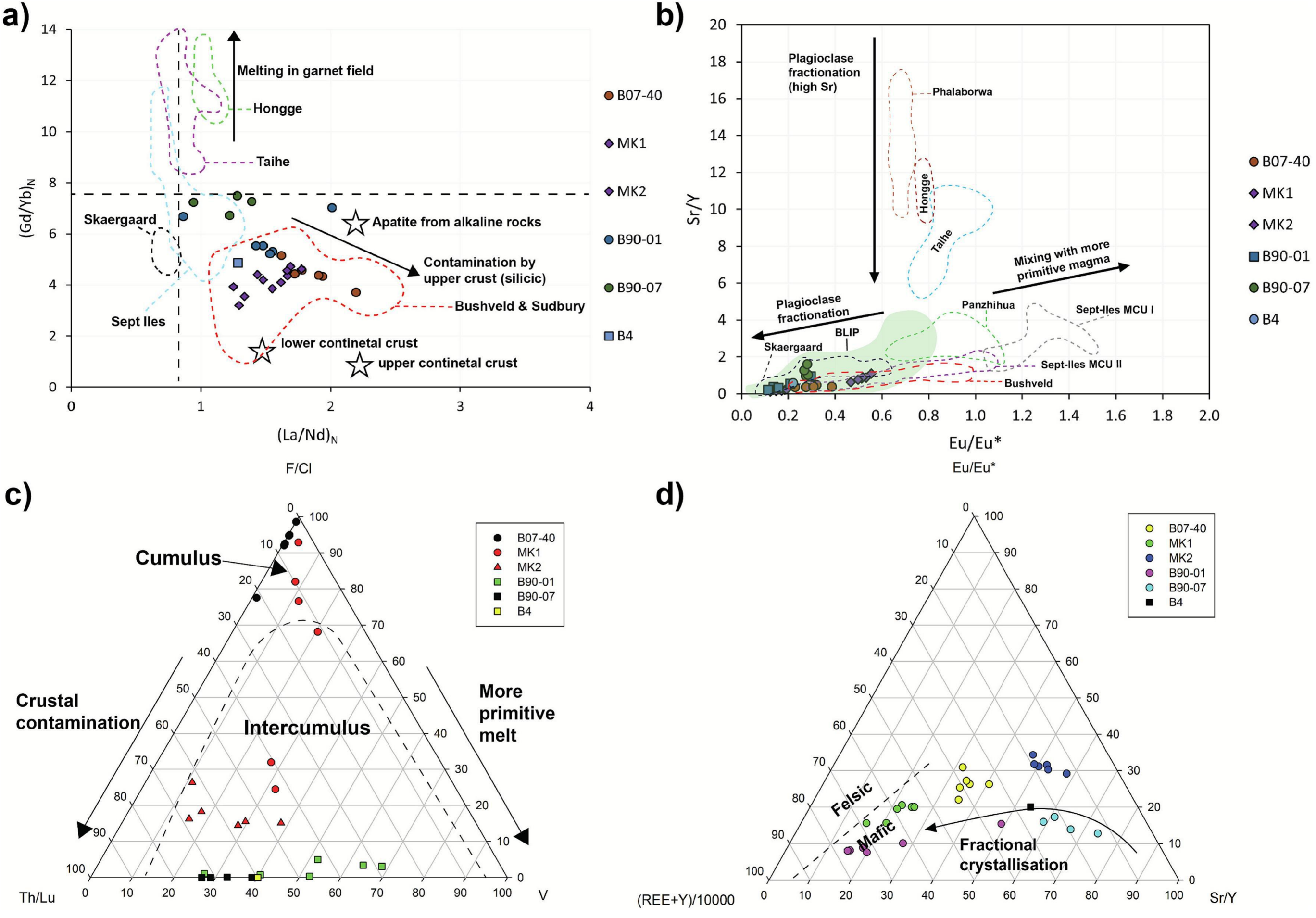
a)
(Gd/Yb)N
(La/Nd)N
0
2
4
6
8
10
12
14
0
1
2
3
4
Melting in garnet field
Hongge
Taihe
Skaergaard
Sept Iles
Apatite from alkaline rocks
Contamination by upper crust (silicic)
Bushveld & Sudbury
lower continetal crust
upper continetal crust
B07-40
MK1
MK2
B90-01
B90-07
B4
b)
Sr/Y
Eu/Eu*
0
2
4
6
8
10
12
14
16
18
20
0.0
0.2
0.4
0.6
0.8
1.0
1.2
1.4
1.6
1.8
2.0
Plagioclase fractionation (high Sr)
Phalaborwa
Hongge
Taihe
Mixing with more primitive magma
Plagioclase fractionation
Panzhihua
Sept-Iles MCU I
Sept-Iles MCU II
BLIP
Skaergaard
Bushveld
B07-40
MK1
MK2
B90-01
B90-07
B4
c)
F/Cl
Th/Lu
V
Cumulus
Intercumulus
Crustal contamination
More primitive melt
0
10
20
30
40
50
60
70
80
90
100
B07-40
MK1
MK2
B90-01
B90-07
B4
d)
Eu/Eu*
(REE+Y)/10000
Sr/Y
Felsic
Mafic
Fractional crystallisation
0
10
20
30
40
50
60
70
80
90
100
B07-40
MK1
MK2
B90-01
B90-07
B4

Figure 9

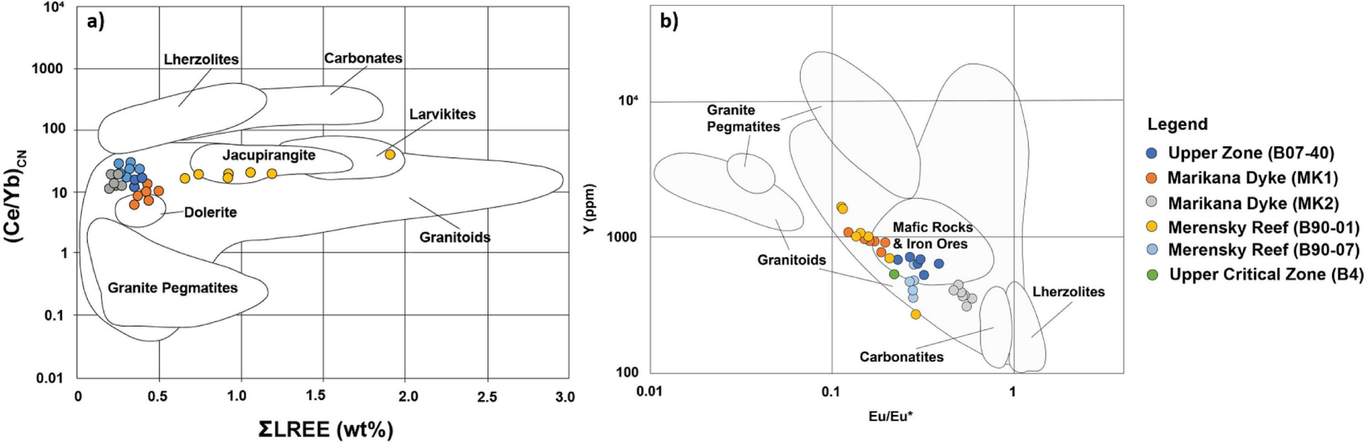
a)
Lherzolites
Carbonates
Larvikites
Jacupirangite
Dolerite
Granitoids
Granite Pegmatites
(Ce/Yb)CN
10⁴
1000
100
10
1
0.1
0.01
0
0.5
1.0
1.5
2.0
2.5
3.0
ΣLREE (wt%)
b)
Granite Pegmatites
Granitoids
Mafic Rocks & Iron Ores
Lherzolites
Carbonatites
Y (ppm)
10⁴
1000
100
0.01
0.1
1
Eu/Eu*
Legend
Upper Zone (B07-40)
Marikana Dyke (MK1)
Marikana Dyke (MK2)
Merensky Reef (B90-01)
Merensky Reef (B90-07)
Upper Critical Zone (B4)

Figure 10

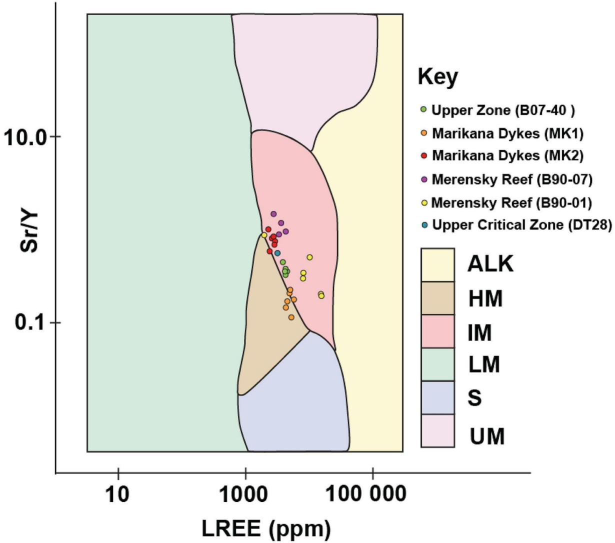
Key
Upper Zone (B07-40)
Marikana Dykes (MK1)
Marikana Dykes (MK2)
Merensky Reef (B90-07)
Merensky Reef (B90-01)
Upper Critical Zone (DT28)
ALK
HM
IM
LM
S
UM
10.0
0.1
Sr/Y
10
1000
100 000
LREE (ppm)

Figure 11

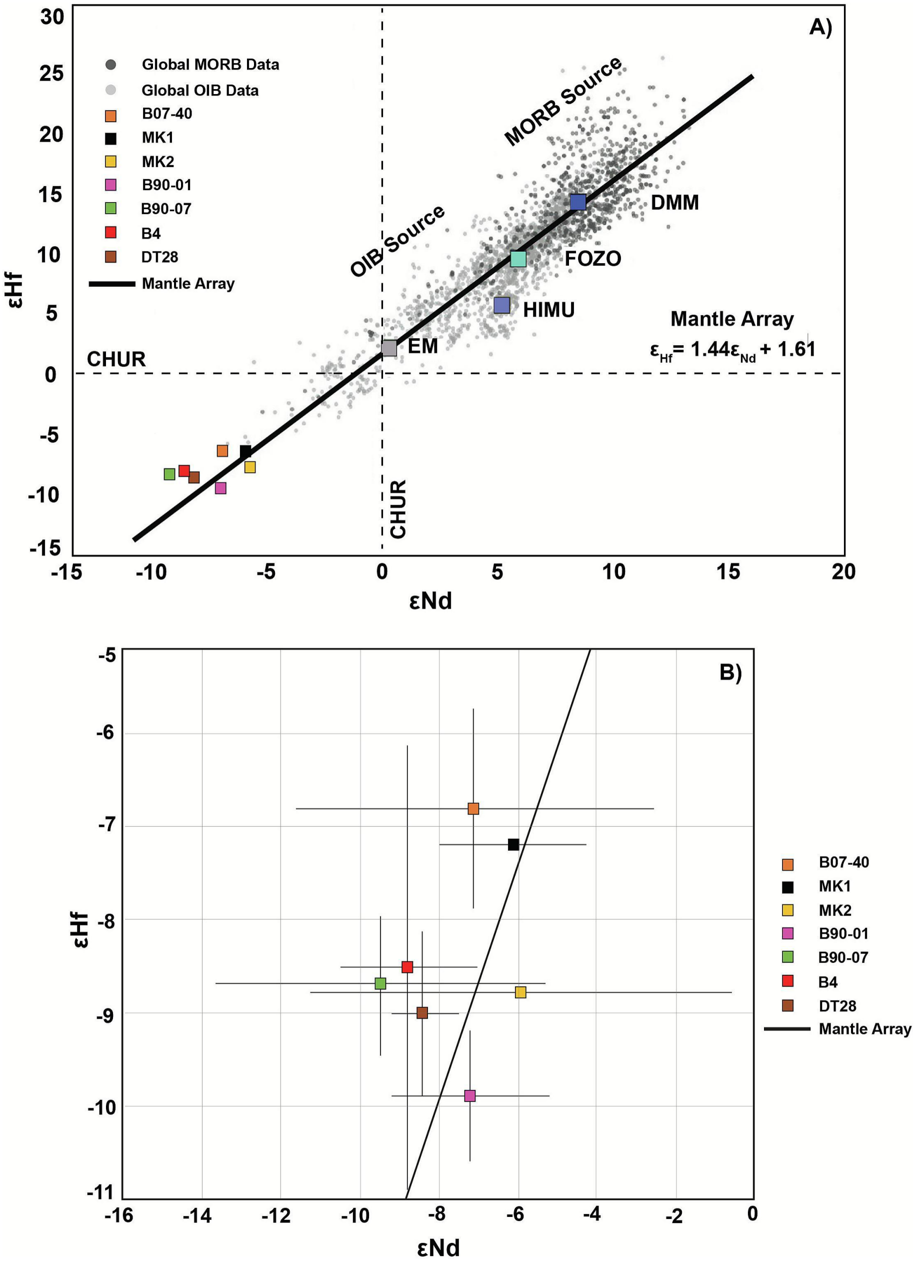
A)
Global MORB Data
Global OIB Data
B07-40
MK1
MK2
B90-01
B90-07
B4
DT28
Mantle Array
MORB Source
OIB Source
DMM
FOZO
HIMU
EM
CHUR
CHUR
Mantle Array
$\varepsilon_{Hf} = 1.44\varepsilon_{Nd} + 1.61$
εHf
30
25
20
15
10
5
0
-5
-10
-15
εNd
-15
-10
-5
0
5
10
15
20
B)
εHf
-5
-6
-7
-8
-9
-10
-11
εNd
-16
-14
-12
-10
-8
-6
-4
-2
0
B07-40
MK1
MK2
B90-01
B90-07
B4
DT28
Mantle Array

Figure 12